

1 **CHARACTERISTICS OF MESOSCALE ORGANIZATION IN WRF**
2 **SIMULATIONS OF CONVECTION DURING TWP-ICE**
3
4
5

6
7 Anthony D. Del Genio*
8 NASA Goddard Institute for Space Studies
9 New York, NY
10

11
12 Jingbo Wu
13 Dept. of Applied Physics and Applied Mathematics, Columbia University
14 New York, NY
15

16
17 Yonghua Chen
18 Dept. of Applied Physics and Applied Mathematics, Columbia University
19 New York, NY
20

21
22
23
24
25
26 Journal of Climate
27 Submitted August 6, 2011
28
29
30
31
32

33
34 * Corresponding Author: Anthony D. Del Genio, NASA Goddard Institute for Space Studies, 2880 Broadway, New
35 York, NY 10025; e-mail anthony.d.delgenio@nasa.gov
36

ABSTRACT

Compared to satellite-derived heating profiles, the Goddard Institute for Space Studies general circulation model (GCM) convective heating is too deep and its stratiform upper level heating too weak. This deficiency highlights the need for GCMs to parameterize mesoscale organization of convection. Cloud-resolving model simulations of convection near Darwin, Australia are used to characterize mesoscale organization processes and provide parameterization guidance. Downdraft cold pools produce upward motions of several m s^{-1} on scales of $\sim 2\text{--}3$ km near the surface and $\sim 5\text{--}6$ km just below cloud base that stimulate further convection. Recovery of cold pool properties to ambient conditions over $5\text{--}6$ hr proceeds differently over land and ocean. Over ocean increased surface fluxes restore the cold pool to pre-storm conditions. Over land the cold pool suppresses surface fluxes; temperature decreases and humidity increases and both then remain nearly constant while the undisturbed environment cools diurnally. The upper troposphere outside the convective updraft area contains a distinct transition region of fairly strong updrafts and buoyant air that appears to be detrained from the convection, and a stratiform rain region of weaker updrafts and buoyancy. Stratiform area and hydrometeor mixing ratio lag convection by $\sim 5\text{--}6$ hr and $\sim 0\text{--}1$ hr, suggesting that the former is controlled by mesoscale dynamics and the latter by detrainment, with mesoscale updraft condensation compensating ice sedimentation. Small stratiform temperature anomalies suggest that a mesoscale updraft parameterization initialized with properties of detrained air and evolving to a balance between diabatic heating and adiabatic cooling might be a plausible approach for GCMs.

1. INTRODUCTION

The problem of representing moist convection in general circulation models (GCMs) has historically used the paradigm of an ensemble of individual convective cells (e.g., Arakawa and Schubert 1974). Ever since the Global Atmospheric Research Program Atlantic Tropical Experiment (GATE) in 1974, however, it has been realized that convective cells are often organized into mesoscale clusters with large precipitating stratiform anvils that evolve differently (Houze and Betts 1981).

Mesoscale convective systems represent only about 10% of all storms in the tropics but account for 80-85% of all rainfall (Del Genio and Kovari 2002). Stratiform rain accounts for much of the raining area and ~40% of the total precipitation in the tropics (Schumacher and Houze 2003). Over the lifecycle of mesoscale clusters, rain evolves from more convective to more stratiform (Houze 1989; Futyán and Del Genio 2007), accompanied by a shift in diabatic heating from first baroclinic mode full-troposphere heating to second baroclinic mode heating in the upper troposphere and cooling below (Houze 1989). This is due to the development of mesoscale updrafts at high altitudes, deposition growth of sedimenting ice particles, melting, and low-level rain evaporation, leading to mesoscale downdrafts (Zipser 1977; Biggerstaff and Houze 1991). This upward shift in heating as stratiform rain increases affects the Walker circulation (Schumacher et al. 2004) and convectively coupled waves (Mapes et al. 2006).

Mesoscale organization of convection is equally important radiatively. Convective storms regulate the tropical planetary albedo and outgoing longwave radiation; 65-75% of their effect comes from mesoscale clusters (Del Genio and Kovari 2002). Mesoscale convective events significantly moisten the upper troposphere (Zelinka and Hartmann 2009). The stratiform rain region and anvil contribute little to water vapor feedback in climate models (Del Genio et al.

1991) but have an important impact on cloud feedback (Yao and Del Genio 1999; Zelinka and Hartmann 2010). The radiative heating profile in the stratiform rain and anvil regions can stabilize/destabilize different altitudes and affect vertical motions (Ackerman et al. 1988; Jensen and Del Genio 2003; Mather and McFarlane 2009; L’Ecuyer and McGarrah 2010;).

Despite their importance, mesoscale updrafts and downdrafts are still not represented in most GCMs, with one exception (Donner 1993; Donner et al. 2001). Many GCMs detrain ice from convective updrafts into anvils, but by itself this is not likely to produce a realistic vertical distribution of heating or its evolution with time.

We demonstrate this using convective heating products retrieved from the Tropical Rainfall Measuring Mission (TRMM) Precipitation Radar. Figure 1 (upper panels) shows two independent estimates of tropical heating composited by precipitable water (PW), from the Convective-Stratiform Heating (CSH) algorithm (Tao et al. 2001) and the Spectral Latent Heating algorithm (Shige et al. 2007). The two represent slightly different quantities (total diabatic heating for CSH; total diabatic minus radiative heating for SLH), but have similar structures, with a transition to a deep heating profile at $PW \sim 45$ mm and a heating peak near 400 hPa at higher PW. The CSH vertical profile has less low level heating than SLH at high PW, and SLH also has a significant shallow convective heating signature at low PW that is weak in CSH, consistent with the findings of Hagos et al. (2010). SLH also separates the heating into convective and stratiform components (Fig. 1, lower panels). The convective heating peaks near 600 hPa and heating rates $> 1 \text{ K d}^{-1}$ reach 350 hPa in the wettest environments. The stratiform component shows the dipole structure seen in field experiments: Upper level heating due to mesoscale updraft condensation and a broad cooling region below the melting level due to melting of snow and evaporation of rain.

Figure 2 shows heating profiles due to parameterized convection and anvils (Del Genio et al. 1996, 2005, 2007) in the Goddard Institute for Space Studies (GISS) Model E2 GCM (Schmidt et al., in preparation). Total heating (upper left panel) resembles that retrieved from TRMM data, especially SLH, but the GCM has more shallow heating and boundary layer cooling than are seen in the retrievals. However, convective heating (upper right panel), and specifically that due to deep convective events (lower left panel), extends much too high. This compensates for almost nonexistent upper level stratiform heating (lower right panel) and a cooling signature that peaks too high and is dominated by melting rather than rain evaporation.

Since the convective and stratiform components dominate at different stages of the lifecycle, the shortcomings in Figure 2 have significant consequences. GCMs consistently produce peak continental precipitation near noon, rather than in late afternoon or evening as observed (Dai 2006). In part this is due to premature triggering of deep convection or weak entrainment (Guichard et al. 2004; Rio et al. 2009; Del Genio and Wu 2010), but the absence of mesoscale organization, which extends the lifetime of convective systems many hours beyond the decay time of individual convective events, prevents significant precipitation later in the day. This error implies that the shortwave effect of convection is biased high (since cloudiness erroneously peaks at low solar zenith angle), while the effect of convection on soil moisture is biased low (since surface rain near noon is more likely to evaporate than infiltrate). The staggered timing of the convective and stratiform heating profiles also affects convectively coupled tropical waves, which in many theories depend on time-varying first and second baroclinic modes (Mapes 2000; Mapes et al. 2006). The most notable evidence of this GCM deficiency is the Madden-Julian Oscillation, which is simulated poorly if at all by most models (Lin et al. 2006; Kim et al. 2009).

Despite the many observational constraints on mesoscale organization from field experiments and satellite data, progress toward parameterization has been elusive. In particular, further insight is required into the relationship between the convection and the organization it spawns. Beyond this, organization is inherently about temporal evolution and thus requires new prognostic variables to represent unresolved quantities whose budgets have not yet been defined. In this paper we use a cloud-resolving model (CRM) to glean information about organization that might form the basis for a future parameterization. Section 2 describes the model and the simulations performed, as well as a classification scheme we employ to characterize different regions of the mesoscale cluster. Organization is a two-part problem. The first involves the downdraft cold pools that generate the next-generation convection which continues the supply of water to the upper troposphere (e.g., Zipser 1977); these are discussed in Section 3. The second part concerns the formation and evolution of the stratiform precipitation region, which we explore in Section 4. In Section 5 we discuss how our results might be used to create a framework for the development of a parameterization of organization in a GCM.

2. MODEL AND SIMULATIONS

a. WRF Model

Our simulations use the Advanced Research Weather Research and Forecasting (WRF) model, version 3.2. WRFV3.2 employs an Eulerian solver for the fully compressible non-hydrostatic equations and complete Coriolis and curvature terms (Skamarock et al. 2008). It uses Arakawa C-grid staggering, and the vertical coordinate is terrain-following dry hydrostatic

1 pressure. The model top is a constant pressure surface. Prognostic variables are in scalar-
2 conserving flux form.

3 Moist convection is resolved in our simulations (Section 2b), which do not use a cumulus
4 parameterization. Subgrid boundary layer turbulence is based on the Mellor-Yamada-Janjic
5 scheme (Janjic, 2002). The parameterization updates the turbulent kinetic energy with the
6 production/dissipation term and the vertical diffusion term from the Mellor-Yamada level 2.5
7 turbulence closure model as extended by Janjic. Exchange coefficients for the surface and all
8 layer interfaces are computed from Monin-Obukhov theory. The land surface is represented by
9 the Noah Land Surface Model (LSM), the successor to the Oregon State University (OSU) LSM
10 described by Chen and Dudhia (2001). Noah is a 4-layer soil temperature and moisture model
11 with canopy moisture and snow cover prediction. It provides sensible and latent heat fluxes to
12 the boundary-layer scheme. Noah also predicts soil ice and fractional snow cover effects, has an
13 improved urban treatment, and considers surface emissivity properties, which are all new since
14 the OSU scheme (Skamarock et al. 2008). The surface layer parameterization is the Monin-
15 Obukhov (Janjic) scheme (Janjic 2002). It generates the surface exchange coefficients for
16 vertical turbulent exchange based upon Monin-Obukhov theory with various refinements.
17 Longwave radiation uses the RRTM (Mlawer et al. 1997), a spectral-band scheme using the
18 correlated-k method. Shortwave radiation is parameterized using the Goddard scheme based on
19 Chou and Suarez (1994). It has 11 spectral bands and considers diffuse and direct solar radiation
20 components in a two-stream approach that accounts for scattered and reflected components.

21 For studying mesoscale convective organization, perhaps the greatest uncertainty is cloud
22 microphysics, especially treatment of the ice phase. We therefore use two very different
23 microphysics parameterizations to distinguish robust features from those that are model-

sensitive. One is the single-moment version of the Morrison et al. (2009) scheme, a bulk scheme that predicts mixing ratios of cloud droplets, cloud ice, rain, snow, and graupel. The other is the Thompson et al. (2008) scheme, which includes the same species but has two-moment cloud ice and rain. The Thompson et al. parameterization is intended for use in winter weather forecasting and aviation applications in which concerns about such things as aircraft icing arise, and it thus focuses more on maintenance of supercooled liquid water than schemes that are designed to simulate convective systems. Differences in the assumptions made by these parameterizations that may affect our results will be discussed at appropriate points later in the paper.

b. Simulation design

We conduct simulations of the active monsoon and monsoon break periods during the Tropical Warm Pool – International Cloud Experiment (TWP-ICE) conducted near Darwin, Australia in 2006 (May et al. 2008). The simulation design is based on that described in Wu et al. (2009) and identical to that of the control run in Del Genio and Wu (2010), who used an earlier version of WRF to study convective updrafts and entrainment. The simulation domain is ~280 km x 280 km centered on Darwin at 600 m resolution with 50 vertical layers and realistic geography. [Bryan et al. (2003) recommend resolution ~100 m for deep convection, but Del Genio and Wu (2010) and Romps and Kuang (2010) find that the coarser resolution produces similar results except for slightly weaker entrainment and mass flux.] The model is driven by European Centre for Medium-Range Weather Forecasts (ECMWF) winds at the boundaries, and temperature and humidity there are updated every 6 hr to match the forcing dataset derived from the TWP-ICE sounding array and constrained variational analysis of Xie et al. (2010).

The active monsoon period of TWP-ICE was characterized by moist westerly flow from ocean to land and extensive, synoptically forced maritime-style convection; simulations of this period are limited by the accuracy of ECMWF winds and the parameterized microphysics, a source of considerable model-to-model variation in the TWP-ICE CRM intercomparison of Varble et al. (2011). The monsoon break period was dominated by easterly winds and unstable but drier conditions. Convection during this period was continental, driven by sea breezes and surface fluxes, which are poorly constrained by TWP-ICE data and not used to force the model. Furthermore, systems often propagated into the domain from the east, which the WRF cannot represent. Our simulations of the break period should therefore be considered semi-idealized portrayals of convective development and not directly comparable to observations.

The active monsoon simulations are initiated at 1200 UT on 19 January 2006 and run until 1200 UT 22 January 2006. The monsoon break simulations begin at 1200 UT on 9 February 2006 and run until 1200 UT 12 February 2006. Both the active monsoon and monsoon break periods are simulated twice, once with the Morrison et al. microphysics and a second time with the Thompson et al. microphysics. Statistics are collected after a 12-hr model spinup period. Except when specified otherwise, figures shown are from simulations with the Morrison et al. microphysics; in such cases runs with the Thompson et al. microphysics behaved similarly.

c. Cloud classification scheme

Figure 3 shows model fields for the active monsoon at 0600 UT 20 January 2006, close to the time of peak model rainfall. On this day Darwin C-POL radar observations indicated a line of convective cells northeast of Darwin, oriented northwest-southeast, with a large stratiform rain region to the south (see the 0300 Z image in Fig. 6 of Varble et al. 2011). The WRF surface

rain rate pattern contains a somewhat similar line of convection at this time, but with a much smaller area of surrounding weaker rain rates (Fig. 3, upper left). The details of such instantaneous storm structures vary considerably from one model to another (Varble et al. 2011).

Since we have direct information about WRF hydrometeor and dynamical fields, we choose to classify convective systems into distinct elements based on that information rather than using simulated reflectivities. We define the deep convective (CU) region in the WRF as those gridboxes with vertical velocity $w > 0$ from below the 750 hPa level to above the 0°C level, with total hydrometeor content $q_h > 0.1 \text{ g kg}^{-1}$. Figure 3 (upper left) shows that this definition generally selects areas within or adjacent to the most heavily raining locations. The definition used by Wu et al. (2009), which required $w > 1 \text{ m s}^{-1}$ and buoyant air, captures only convective cores and results in a smaller convective area less suited to our current purposes.

We define the stratiform rain (SR) region as gridboxes that do not satisfy the CU velocity and cloud base constraints but whose tops lie above the 0°C level and whose surface precipitation rates (P) lie in the range $5 > P > 0.5 \text{ mm hr}^{-1}$ with $q_h > 0.1 \text{ g kg}^{-1}$. The upper bound is commonly used in convective-stratiform partitioning studies (see, e.g., the discussion in Schumacher and Houze 2003), while the lower bound is roughly the weakest rain rate detected by satellite rain instruments. This leaves a significant area with $P > 5 \text{ mm hr}^{-1}$ that falls into neither the CU nor SR category. Cross-sections through the primary convective region show that although CU locations often have strong updraft speeds and large amounts of condensate, such properties are not exclusive to those locations (middle and lower panels of Figure 3); there are numerous gridboxes with similar properties in the upper troposphere, often close to the convective updrafts. Rain radar studies often define a separate “transition” region between the convective and stratiform parts of a cluster with intermediate rain rates (e.g., Atlas et al. 1999) and sometimes a

1 minimum in reflectivity (e.g., Braun and Houze 1994). It is not clear whether such areas should
 2 be considered part of either the convective or stratiform region (see the discussion in
 3 Schumacher and Houze 2003), so we opt to define a separate “transition rain” (TR) category,
 4 analogous to the SR definition but with $P > 0.5 \text{ mm hr}^{-1}$. We argue later that the TR region has
 5 distinct dynamic and thermodynamic properties relevant to the parameterization of organization.

6 Figure 3 (upper right) shows the resulting classification, with TR regions indeed
 7 primarily surrounding CU gridboxes and adjacent to SR areas. Table 1 shows the area covered
 8 by convective and stratiform rain in the model vs. those derived from TWP-ICE C-POL radar
 9 data by Frederick and Schumacher (2008). Frederick and Schumacher do not define a separate
 10 TR region, but their convective-stratiform separation (based on reflectivity patterns) defines high
 11 reflectivity regions ($\sim 10 \text{ mm hr}^{-1}$ or higher rain rate) as convective; the most straightforward
 12 comparison is thus with the sum of our CU and TR areas. Given that Frederick and Schumacher
 13 use a different classification scheme, averaged over a longer time and slightly smaller area (the
 14 120 km radius C-POL field of view) than ours, the agreement between model and data is
 15 reasonable. WRF slightly overpredicts raining area during the active period and underpredicts it
 16 during the break period; the active period raining area lies within the range of the CRMs
 17 analyzed by Varble et al. (2011). The Morrison et al. microphysics simulates larger TR and SR
 18 areas than the Thompson et al. microphysics for both periods. This may be due to differences in
 19 their particle size distributions. Morrison et al. use a Marshall-Palmer distribution for rain, with
 20 a constant intercept in the single-moment version. Thompson et al. instead use a gamma
 21 distribution with a variable intercept and slower fall speeds (their Fig. A1) and thus get a smaller
 22 area that exceeds our rain thresholds for TR and SR. The simulated stratiform/convective area
 23 ratio is somewhat larger than observed in both periods for both microphysics schemes.

3. DOWNDRAFT COLD POOLS

Most GCMs parameterize convective downdrafts, which maintain boundary layer quasi-equilibrium by transporting low moist static energy air from the middle troposphere (Emanuel et al. 1994). Historically, cumulus parameterizations have instantaneously mixed downdraft air that enters the boundary layer with ambient air there, which stabilizes the column and suppresses further convection. Previous studies have suggested, however, that cold pools that form from downdraft descent remain distinct for hours. As they spread over time and organize convergence and high moist static energy at the gust front, further convection is promoted rather than suppressed (Zipser 1977; Mapes 2000; Tompkins 2001; Khairoutdinov and Randall 2006).

The TWP-ICE break period is most conducive to exploring cold pools, since convection is more localized and the cold pools more limited in area and distinct from other locations. Figure 4 shows the evolution of surface rain rate and temperature during one afternoon. The temperature color bar is chosen so that red/blue distinguish the land and ocean surfaces before precipitation first reaches the surface over the mainland in the southern half of the domain. After mainland rain begins (04 UTC), small pockets of cooler surface air can be seen at the rain locations, which expand to become distinct cold pools by 06 UTC, when the rain rate peaks. The cold pools continue to expand (at a mean rate of $\sim 3\text{--}4\text{ m s}^{-1}$) as rain weakens at 08 UTC, eventually covering an area comparable to a climate GCM gridbox, until the undisturbed land surface cools in early evening (10 UTC = 7:30 PM) to a temperature similar to the cold pool.

The coastal geography of Darwin is a complicating factor for our simulations, but it has one advantage – the cold pools that form over the mainland eventually spread out over the adjacent ocean. This allows us to diagnose how cold pool recovery proceeds separately over land and ocean for the same convective event. Based on Figure 4, the land cold pool is easily

identifiable during daytime as areas with temperature $< 31^{\circ}\text{C}$. The ocean cold pool is more difficult to isolate since the sea surface is cooler than the undisturbed land surface. We find that if we restrict ourselves to the area south of the Tiwi Islands ($y < 40$ km) and exclude a small area of cooler ocean along the west coast of the mainland ($x < -60$ km), a criterion of temperature $< 29^{\circ}\text{C}$ satisfactorily identifies the ocean cold pool gridboxes.

The resulting temporal evolution of the cold pools is different over ocean and land (Fig. 5). Cold pools do not reach the ocean surface until shortly after 4:00 PM. When they do, ocean surface air temperatures and humidities in the cold pool locations are $\sim 1.5^{\circ}\text{C}$ colder and $\sim 1 \text{ g kg}^{-1}$ drier than elsewhere. This leads to a sharp increase in surface sensible and latent heat fluxes that gradually restore the cold pool air to ambient characteristics over the next ~ 3 hr while the surface fluxes relax back to pre-cold pool values. This progression was also shown by Tompkins (2001).

Over land, cold pool evolution is different. Continental cold pools are first detected at $\sim 1:00$ PM, at which time surface air temperature is quickly depressed by ~ 4 K and surface humidity increased by $\sim 2 \text{ g kg}^{-1}$. Unlike the ocean case, however, the low thermal inertia land surface cools in response to the colder air above it. Surface sensible heat flux thus rapidly decreases and is not able to restore the surface air to pre-cold pool conditions. Meanwhile the latent heat flux gradually decreases as well. The net result is that the initial surface air temperature and humidity anomalies persist until early evening, by which time the undisturbed land surface cools diurnally to a temperature similar to that of the cold pool and the cold pool/non-cold pool distinction disappears. (The cold pool does remain wetter than its surroundings through the night.) Surface air temperature data during the break period at the Howard Springs station show similar behavior (Fig. 6) in response to the passage of a storm (see Fig. 11 c,d of Frederick and Schumacher 2008) at ~ 2200 LST (1230 UTC) on 10 February, with an immediate

cooling of $\sim 3\text{--}4^\circ\text{C}$ and then nearly constant temperature until 600 LST on 11 February, when the normal downward diurnal temperature progression resumes.

Vertical velocity at the time of peak rainfall at 600 m and 2 km altitude, the latter close to the mean cloud base, is shown in Figure 7. Strong updrafts ($> 1 \text{ m s}^{-1}$) are found almost exclusively in curved arcs surrounding locations of current and previous heavy rain (Fig. 4), suggesting an origin at cold pool gust fronts. Strong downdrafts exist just inside these arcs, marking the presumed source of the cold pools. The spatial scale of strong upward motions at 600 m altitude is several km, somewhat larger than the typical turbulent eddies that arise over land earlier in the day before cold pool onset (not shown). At 2 km altitude, the gust front eddies have expanded in scale to ~ 10 km, with upward motions of $4\text{--}5 \text{ m s}^{-1}$ in some locations.

4. MAINTENANCE OF THE STRATIFORM RAIN REGION

a. Characteristics of the CU, TR, and SR regions

Figure 8 shows the evolution of temperature anomalies in the TR (upper) and SR (lower) regions for simulations with the two microphysics schemes. TR upper troposphere air is buoyant by up to $0.5\text{--}1^\circ\text{C}$, suggesting that it originated via detrainment from buoyant CU updrafts. Sharp transitions to cool anomalies are sometimes present near the 0°C level (545 hPa), indicating melting of falling ice, and more so for the run with the Morrison et al. microphysics. The major instances of such cooling (~ 06 UTC each day) are accompanied by cool anomalies through part or all of the lower troposphere, with air several degrees colder than average near the surface. This suggests that the TR region is where convective downdrafts and cold pools are initiated.

The SR region is somewhat different. Upper troposphere temperature anomalies are no

more than several tenths of a degree and are occasionally cool rather than warm, i.e., SR is close to neutrally buoyant. Melting level negative anomalies are small but consistent in time. Lower troposphere anomalies are similarly small, and with one exception, surface cold pools are absent.

Figure 9 shows probability distributions of vertical velocity for the active monsoon. CU velocities (left panels) are several m s^{-1} , similar to those observed in oceanic (Zipser and Lutz 1994) and Darwin active monsoon (May and Rajopadhyaya 1999) convection. (The updraft speed pdf differs from that in Wu and Del Genio (2009), in part because that paper used an earlier version of WRF with different parameterizations, but primarily because here we use a more liberal definition of convective updraft gridboxes that does not isolate convective cores.) CU pdfs below the melting level are similar in the runs with the two different microphysics parameterizations but differ above, especially the strongest (99th percentile) updrafts. Strong updrafts in the Morrison et al. run strengthen from the melting level to ~ 400 hPa and then weaken above, while those in the Thompson et al. run slightly weaken above the melting level and then strengthen from ~ 400 hPa to ~ 200 hPa. A possible reason for this is the differing treatment of graupel in the two schemes. Morrison et al. use fixed hydrometeor mixing ratio thresholds for forming graupel and allow graupel to form from collisions between rain-snow, rain-cloud ice, and snow-cloud liquid particles. Thompson et al. form graupel only from collisions between snow and cloud liquid when riming growth is faster than depositional growth, consistent with their desire to maintain supercooled liquid water. Consequently, ice formation (and latent heat release, which increases buoyancy) in the Thompson et al. run occurs primarily at temperatures far below 0°C , where primary ice nucleation and heterogeneous or homogeneous freezing occur, whereas the greater graupel formation in the Morrison et al. run, which occurs primarily at warmer temperatures, accelerates parcels within a few km above the melting level.

SR vertical velocities (Fig. 9, right panels) are both positive and negative at all altitudes, but the mean is positive (negative) above (below) the melting level, as expected. Mesoscale updraft velocities are tens of cm s^{-1} and mesoscale downdrafts slightly weaker, consistent with field experiments (Houze 1989). The SR vertical velocity distributions are less sensitive to the choice of microphysics than those in the CU region. TR updraft speeds are not surprisingly intermediate between those of the CU and SR regions. The mean TR updraft speed in the upper troposphere is only slightly stronger than its SR counterpart, but the upper 10% of velocities are several m s^{-1} , again suggesting that the TR region contains detrained CU air.

Vertical velocities during the break period (not shown) are stronger, peaking (99th percentile) at 25-30 m s^{-1} near 200 hPa in the CU region for both microphysics schemes. In general the strongest updrafts in all three regions are somewhat stronger in the Thompson et al. simulation, but otherwise the vertical velocities are less sensitive to the choice of microphysics.

The vertical profiles of hydrometeor species for the active monsoon are shown in Figure 10. Convective rain profiles are almost identical for the two microphysics schemes, peaking at 0.9 g kg^{-1} at ~700 hPa, decreasing to zero at ~450 hPa, and with a mixing ratio of 0.6 g kg^{-1} at the surface. Otherwise the effect of different microphysics is large. The most striking difference is the large amount of snow produced by the Thompson et al. microphysics relative to Morrison et al.. This was also noted by Wu and Petty (2010) for a very different climate regime (polar lows). They attribute the difference to the assumed size distributions. The single-moment Morrison et al. scheme assumes a Marshall-Palmer distribution for snow with a constant intercept. Thompson et al. use the sum of a Marshall-Palmer and a gamma distribution to simulate the “superexponential” number concentration of small particles reported in some observations; this implies slower fall speeds overall, and thus a greater buildup of snow via

1 deposition. Cloud ice is almost nonexistent in the Thompson et al. run relative to the Morrison et
2 al. run, but this may be something of an artifact, given that the “superexponential” size
3 distribution of snow used by Thompson et al. includes sizes usually categorized as cloud ice.

4 As noted earlier, Thompson et al. suppress graupel formation when depositional growth
5 is rapid, so the simulation with this microphysics contains only a modest amount of graupel in
6 the CU region, less in the TR region, and almost none in the SR region. This is consistent with
7 the greater fall speed of graupel relative to other ice particles and the weakening of updraft speed
8 from the CU to TR to SR region. It is qualitatively realistic compared to observations of African
9 squall lines, which show some graupel adjacent to convection but little in the far-removed
10 stratiform area (Bouniol et al. 2010; Cetrone and Houze 2011). The Morrison et al. run,
11 however, produces apparently excessive graupel, with concentrations comparable to snow in the
12 CU and TR regions and non-negligible even in the SR region. Overestimation of graupel is a
13 chronic problem for many CRMs (Varble et al. 2011). The suppression of riming in the
14 Thompson et al. scheme naturally has the opposite effect on cloud liquid water: peak cloud liquid
15 mixing ratios near the melting level are greater in this simulation than in the Morrison et al. run.

16 Hydrometeor profiles during the break period (not shown) are similar in most respects
17 but differ from those for the active period in several ways that reflect the stronger convection
18 during the break period and exaggerate differences between the two microphysics schemes.
19 Thompson et al., while producing 2-3 times more graupel in the CU region during the break
20 period than in the active period, is still dominated by snow at upper levels, whereas the Morrison
21 et al. break period run actually has much more graupel than snow in the CU and TR regions, and
22 comparable graupel and snow in the SR region. Rain water peaks during the break period at
23 ~600 hPa with a mixing ratio of $\sim 2 \text{ g kg}^{-1}$ for both microphysics schemes.

b. Relationships between TR/SR properties, the environment, and parent convection

The extent to which convection organizes into mesoscale clusters with long lifetimes depends on environmental factors such as humidity and wind shear that promote “sustainability” (Yuter and Houze 1998; Schumacher and Houze 2006). Differences between the TWP-ICE active and break periods are suggestive of differences in sustainability. During the active monsoon relative humidity (RH) was 90-95% from the surface to the upper troposphere, whereas the break period had only 80-85% RH in the boundary layer, decreasing to ~60% in the free troposphere (Fig. 1 of Wu et al. 2009). The much larger SR area during the active period (Table 1) is thus consistent with an environmental humidity control on organization. During the active monsoon, large-scale upward motion creates a positive moisture tendency (Xie et al. 2010) that keeps humidity high and sustains convection. During the break period, however, there is little low-level moisture tendency, so convection is only maintained by surface fluxes. Downdraft cold pools initially trigger new convection (Fig. 4) but suppress surface fluxes over land, so as the cold pool spreads and the undisturbed environment cools diurnally, convection ceases.

A separate question is whether upper level humidity influences the evolution of the stratiform region once it forms. Figure 11 (upper panels) shows lag correlations between 600-200 hPa domain mean RH and TR or SR area for the active period. TR area is uncorrelated or weakly negatively correlated with RH, consistent with control by detrainment, not the environment. SR area is moderately correlated with RH at zero lag but less so at longer lags. Neither TR nor SR area is significantly correlated with RH during the break period (not shown). We also examined correlations with 600-200 hPa wind shear, which were negligible during the break period (not shown) but statistically significant during the active period (Fig. 11, lower panels) at lags of 2-3 hr (Morrison et al. microphysics) or 5-6 hr (Thompson et al. microphysics).

1 The immediate question for a parameterization, however, is: given deep convection, how
 2 should a stratiform rain region and anvil develop from it? A central question motivating TWP-
 3 ICE was whether properties of stratiform clouds accompanying convection are related to the
 4 convection itself (mass flux, area, updraft speed, hydrometeor content). Cumulus mass flux is
 5 the best predictor of the TR and SR areas in our simulations, but in different ways at different
 6 times (Fig. 12). TR area is highly correlated with cumulus mass flux for both the active and
 7 break periods and for both microphysics schemes at a lag of 0-1 hr and decreases sharply
 8 thereafter, again consistent with a detrainment source. SR area during the break period is also
 9 highly correlated with cumulus mass flux but with a 1-2 hr lag and also decreasing sharply for
 10 longer lags, suggesting that in the drier, less sustainable break period environment, the stratiform
 11 rain region is simply the onset of the decaying stage of the cluster as convection and detrainment
 12 terminate – similar to the way most GCMs currently treat convection, with no mesoscale *in situ*
 13 source of upward motion and little stratiform heating (e.g., Fig. 2). During the active period,
 14 though, SR area is moderately to highly correlated with cumulus mass flux only at long lags (5-6
 15 hr or more), suggesting that detrained air serves as a trigger that provides ice crystals to the
 16 humid environment which then grow by deposition as they sediment, releasing latent heat and
 17 eventually generating their own mesoscale updraft which maintains the stratiform rain for hours.

18 Combining Figures 11 and 12, the following tentative story emerges. A humid upper
 19 troposphere is important at the outset to allow convection to fully deepen and to provide a
 20 nurturing environment for detrained ice crystals. Given this, wind shear may spread the
 21 stratiform area for several hours beyond that, but full *in situ* development of a mesoscale updraft
 22 requires considerable time yet depends for its initiation on the ice initially detrained many hours
 23 earlier. Note that the microphysics matters: The SR area responds to cumulus mass flux more

quickly and strongly with the Thompson et al. microphysics, perhaps since its glaciation is more restricted to higher colder altitudes where ice can more efficiently grow by deposition.

TR hydrometeor water content is almost perfectly correlated with CU hydrometeor water content at 0-1 hr lag for both the active and break periods and both microphysics schemes and decreases at longer lags (not shown), consistent with our previous inferences about this region. SR hydrometeor content behaves similarly during the break period but has lower peak correlations during the active period, especially with the Morrison et al. microphysics, consistent with an important role for *in situ* ice formation then. The highest correlations for SR hydrometeor content are with cumulus mass flux at 0-1 hr lag and cumulus updraft speed at lags of 2-3 hr (Fig. 13). Again, these correlations are somewhat higher for the Thompson et al. microphysics, perhaps because of its slower ice fall speeds. Updraft speeds in both regions are generally highly correlated with both cumulus updraft speed and cumulus mass flux at 0-1 hr lag (not shown), slightly more so for the TR region than the SR region during the active period, although the correlations are noticeably lower for the Thompson et al. break period run.

5. DISCUSSION

The behavior we have described illustrates the parameterization challenge of convective organization – the evolution of a convective system over its lifecycle of many hours cannot be diagnosed from current large-scale thermodynamic and/or dynamic conditions, as cumulus parameterizations conventionally assume. Organized convection has memory; at today's climate model resolutions (~100-200 km) it is still largely subgrid-scale, but the present state of a convective cluster depends on the behavior of subgrid-scale parameters at previous time steps.

A successful parameterization of organization must capture 3 stages of cluster evolution (Futyan and Del Genio 2007): (1) A developing stage in which rain begins, convection deepens and cluster area grows; (2) a mature stage in which the cluster is at its maximum depth but is still expanding in area, and during which rain rates peak; (3) a dissipating stage in which the depth, area, and rain rate decrease, convection weakens and then terminates, and only stratiform rain remnants remain. Stage 1 depends on cold pool formation, its effect on convective triggering and entrainment, and anvil initiation by detrainment. Stage 2 is controlled by the sustainability of convection, including the physics of the mesoscale updraft and downdraft. Stage 3 depends on the factors that first terminate convection and then terminate stratiform rain. We consider each of these in turn to suggest a possible simple framework for parameterization.

a. Cold pools

Several parameterizations of cold pools and their effect on subsequent convection have already been proposed, from detailed models of cold pool dynamics with many prognostic variables (Qian et al. 1998; Grandpeix and Lafore 2010) to a simple approach with a single abstract prognostic variable *org* representing the extent of organization (Mapes and Neale 2011).

A GCM really only needs to know two things about cold pools: Areal extent (how much undisturbed air remains in a gridbox and whether a cold pool spreads to neighboring gridboxes) and the contrast between cold pool properties and the undisturbed environment. Thus a simple parameterization might be based on prognostic equations for cold pool area, temperature and humidity. To a first approximation, cold pool area increases at the rate at which downdraft air is injected into the boundary layer. The detailed parameterizations mentioned above also account for entrainment and the time-varying tradeoff between depth and area determined by the cold

pool – environment density difference (which determines gravity current speed). However, in the WRF (Fig. 8, lower panels) and in parameterization tests (Grandpeix et al. 2010), cold pool depth does not vary significantly over much of its lifetime. Thus, one might specify a constant cold pool depth, proportional to the virtual potential temperature (θ_v) difference between the entering downdraft air and the environment, which explains much of the difference in cold pool behavior over land and ocean (Rozbicki et al. 1999; Grandpeix et al. 2010). Given the large uncertainty in current GCM downdraft parameterizations, such an intermediate approach seems appropriate. A cold pool that occupies the entire gridbox would end convection there but might be advected with the prevailing wind to a neighboring gridbox to propagate the cluster.

Cold pool temperature and moisture also seem amenable to simple approaches, based on Figure 5. Over ocean, a simple forcing-damping approach such as that used for *org* by Mapes and Neale (2011), with forcing by the downdraft mass flux and a linear damping with a specified time scale (~ 4 -5 hr based on our Fig. 5 and Qian et al 1998) could represent the onset and then the restoring effects of surface turbulent fluxes. Over land the cold pool suppresses surface fluxes, so temperature and humidity can be assumed constant over its lifetime (Fig. 5). Termination of the cold pool over ocean would occur when cold pool θ_v had relaxed to that of the undisturbed environment, while termination over land would occur instead when the undisturbed land surface air had cooled to the cold pool θ_v (e.g., bottom right panel of Fig. 4).

b. Convective triggering and entrainment

There are several ideas about how cold pools promote convection onset. Most popular is the idea that convergence at the gust front organizes upward motion on larger scales than that of normal turbulence, thus creating larger air parcels that entrain less (Kuang and Bretherton 2006;

1 Khairoutdinov and Randall 2006). Others suggest that the convergence itself is required to lift
 2 parcels to their level of free convection (Grandpeix and Lafore 2010).

3 Figure 7 shows that air rising at the gust front grows from 2-3 km in scale, somewhat
 4 larger than that of turbulence, to ~5-6 km between 600 m and 2 km altitude. The mass flux of a
 5 convective cloud with many subcloud parcels varies with height due to competition between
 6 entrainment and detrainment. Shallow convective clouds are weakly buoyant and rapidly detrain
 7 as they rise, so their mass flux and area decrease with height (de Rooy and Siebesma 2008).
 8 Deep convection is more buoyant, so entrained air largely remains buoyant, detrainment is weak,
 9 and mass flux increases with height in the first few kilometers (e.g., Xie et al. 2002). Thus, if
 10 gust front air reduces entrainment by producing bigger parcels, growth of parcel “radius” with
 11 height may be why. This could be accommodated in existing parameterizations, but it requires
 12 finding the right balance between entrainment and detrainment. Del Genio and Wu (2010) did
 13 find that a larger fraction of the buoyant turbulent kinetic energy generation in convective
 14 updrafts was used for entrainment (in the context of one particular parameterization) at low
 15 altitudes than in the middle troposphere in an earlier WRF TWP-ICE simulation, consistent with
 16 the increase of cumulus mass flux with height near cloud base.

17 Another possible reason for decreased entrainment is the large updraft speeds at the gust
 18 front, which imply that rising air spends less time per unit distance of rise subject to entrainment.
 19 Updraft speeds are larger in the high moist static energy air near cloud base after the onset of
 20 deep convection than before (Del Genio and Wu 2010). Updraft speeds $> 1 \text{ m s}^{-1}$ at 2 km
 21 altitude in our simulations occur only at the gust front (Fig. 7). The parameterization of Gregory
 22 (2001), which is used in the GISS GCM, produces weaker entrainment in deep convection than
 23 in shallow convection because it varies as $1/w^2$ (Del Genio and Wu 2010). Romps and Kuang

(2010) find that the average vertical distance between individual entrainment episodes increases from ~200 m in shallow convection to 540 m in their CRM study. Piriou et al. (2007) propose an entrainment scheme with memory using a prognostic equation for the probability of undiluted updrafts at a given level that increases with rain evaporation.

A third possible reason for deep convection to be less affected by entrainment is that updrafts entrain air that is more humid than the rest of the environment due to pre-conditioning by detrainment from earlier-generation plumes (Mapes and Neale 2011). Figure 14 shows the cloud classification and 600 hPa RH field during our active and break WRF simulations. During the active period (upper panels) the environment is nearly saturated, and the air surrounding the convective updrafts is actually slightly drier in some places (see also Table 2), perhaps due to downdrafts. However, during the drier break period (lower panels) the area of very humid air is clearly broader than that of the updrafts, covering most of the TR area, presumably due to rain evaporation and the transfer of air out of the cloud during earlier detrainment episodes. On average TR air entrained into convective updrafts is 12% drier than the air inside the CU region, but 16% *wetter* than the domain mean RH (Table 2). Thus, the *efficacy* of entrainment – its ability to reduce parcel buoyancy – is reduced in the vicinity of deep convective clouds. Such “humidity halos” have been observed adjacent to shallow cumulus clouds (e.g., Laird 2005).

c. Mesoscale updrafts and downdrafts

To our knowledge the only attempt to represent mesoscale updrafts and downdrafts in a GCM is the scheme of Donner (1993) and Donner et al. (2001), but their mesoscale vertical velocities are prescribed and applied at the same time as the convection and thus do not simulate

lifecycle evolution. To add memory, a parameterization must represent the mesoscale energy and moisture budgets and the evolution of vertical velocity, area and hydrometeor mixing ratio.

Figure 8 suggests a simple approach to the mesoscale energy budget. Air in the TR region is significantly buoyant, suggesting that it is detrained from the CU region; this is also supported by its spatial relationship to the CU region (Fig. 3), the several m s^{-1} peak updraft speeds there (Fig. 9), and the consistent correlation of its properties with those of the CU region with small lags (Figs. 12-13). On the other hand, SR region air is only weakly buoyant (Fig. 8), consistent with its much weaker updraft speeds (Fig. 9). We might therefore assume that the mesoscale temperature tendency has a source term from buoyant rising detrained air that initializes the parameterized mesoscale updraft speed ω_m (see, e.g., Section 9.2 of Houze 1993). This initiates condensation and latent heating through vertical advection of moisture from the base of the detrained air, as well as radiative heating/cooling. At later timesteps, diabatic heating and adiabatic cooling add to the temperature tendency until convection and detrainment terminate, and then future evolution of ω_m is computed from a balance between adiabatic cooling and diabatic heating. A similar equation is not required for the moisture budget of the mesoscale updraft because the condensation term can assume saturation at the cloud base temperature. Likewise, the mesoscale downdraft can be computed from a balance between evaporation cooling and subsidence warming after an initial cooling source from melting and perhaps sublimation due to horizontal advection of dry air into the SR region from the environment to represent the effect of the often-observed rear inflow (Houze 2004).

The area of the mesoscale SR region must also be prognostic. We interpret the significant lag between cumulus mass flux and SR area in the active period, and the absence of a large lag during the break period (Fig. 12), as evidence that in the drier break period environment

(~55% RH with respect to water in the upper troposphere), the SR region is restricted to whatever detrainment occurs, and that detrained ice sublimates. During the active period, though, when upper troposphere RH is almost water-saturated, detrainment initiates a mesoscale updraft at ~200-400 hPa; the sedimenting ice grows further by deposition, extending the stratiform cloud and mesoscale updraft down to the melting level. The 5-6 hr lag we see in Fig. 12 (upper panels) then represents the time it takes for the mesoscale updraft to develop and equilibrate over its entire depth. Thus the peak correlation of active period SR area with RH at zero lag (Fig. 11) indicates the role of upper level RH as a gatekeeper that controls whether deposition that leads to anvil growth can even begin, i.e., “sustainability.” In a GCM this should be determined by the parameterized microphysics. A prognostic equation for SR area might then include source terms due to convective detrainment and spreading by wind shear (Fig. 11, lower panels), offset by a sink initiated when ice loss by sedimentation begins to outweigh deposition growth.

Finally, a prognostic equation for mesoscale region hydrometeor water content should have ice detrainment as its primary source, given that the correlation between convection strength and mixing ratio peaks at short lags (Fig. 13). Competition between a second source due to deposition in the mesoscale updraft and ice sedimentation then determines the evolution after convection ceases. (Note that snow is not a prognostic variable in current GCMs, which prevents them from even creating a mesoscale anvil whose base extends down to the melting level.) Once the mesoscale updraft source disappears, the remaining ice could be transferred to the GCM’s stratiform cloud parameterization, which in most models is already prognostic and would thus treat the non-precipitating anvil (Li and Schumacher 2010; Yuan and Houze 2010).

Since ω_m is controlled thermodynamically by detrainment and diabatic heating, there is no requirement that the deposition source balance the sedimentation sink of ice in the condensed

1 water budget. Instead, this balance will be sensitive to the parameterized microphysics. A useful
2 test of GCM microphysics might then be whether (a) organization produces a lifecycle of
3 developing, mature, and dissipating stages as seen in satellite data (Futyan and Del Genio 2007),
4 (b) the stratiform heating/cooling pattern resembles TRMM retrievals (Fig. 1), and (c) the
5 mesoscale updraft speeds are stronger than grid-scale vertical motions but weaker than the fall
6 speed of snow, the defining characteristic of the stratiform region (Biggerstaff and Houze 1991).

7
8 The outline described above should be regarded as the basis for a first attempt to capture
9 some of the characteristics of mesoscale organization of convection in a GCM. It is primarily
10 thermodynamic in nature and ignores in particular issues associated with the various
11 morphologies that clusters can have in different low-level shear environments and the role of the
12 momentum budget. Our results were derived only for two different environments and two
13 microphysics parameterizations in a single CRM structure. Similar experiments should be
14 performed with other CRMs and in other climate regimes to determine how robust the behavior
15 we report is. New opportunities for observation of the microphysics and dynamics of mesoscale
16 clusters also now exist with the advent of arrays of Doppler radars and lidars that can better
17 constrain 3-dimensional cloud and rain structure and its temporal evolution, as well as the
18 dynamics and microphysical properties of the clouds. Recent examples of these new capabilities
19 such as the Mid-latitude Continental Convective Clouds Experiment
20 (<http://campaign.arm.gov/mc3e/> and <http://mc3e.nsstc.nasa.gov/>) promise to provide useful tests
21 for both CRMs and GCM parameterizations that are based on them.

1 **ACKNOWLEDGEMENTS.** This research was supported by the NASA Precipitation
2 Measurement Missions Program, the DOE Atmospheric Systems Research and FASTER
3 programs, and the NASA Modeling and Analysis Program.

4

5

REFERENCES

- Ackerman, T.P., K.-N. Liou, F.P.J. Valero and L. Pfister, 1988: Heating rates in tropical anvils. *J. Atmos. Sci.*, **45**, 1606-1623.
- Arakawa, A., and W.H. Schubert, 1974: Interaction of a cumulus cloud ensemble with the large-scale environment, Part I. *J. Atmos. Sci.*, **31**, 674-701.
- Atlas, D., C.W. Ulbrich, F.D. Marks Jr., E. Amitai and C.R. Williams, 1999: Systematic variation of drop size and radar-rainfall relations. *J. Geophys. Res.*, **104**, 6155-6169.
- Biggerstaff, M.I., and R.A. Houze, Jr., 1991: Kinematic and precipitation structure of the 10-11 June 1985 squall line. *Mon. Wea. Rev.*, **119**, 3034-3065.
- Bouniol, D., J. Delanoë, C. Duroure, A. Protat, V. Giraud and G. Penide, 2010: Microphysical characterisation of West African MCS anvils. *Q.J.R. Meteorol. Soc.*, **136**, 323-344.
- Braun, S.A., and R.A. Houze Jr., 1994: The transition zone and secondary maximum of radar reflectivity behind a midlatitude squall line: Results retrieved from Doppler radar data. *J. Atmos. Sci.*, **51**, 2733-2755.
- Bryan, G.H., J.C. Wyngaard and J.M. Fritsch, 2003: Resolution requirements for the simulation of deep moist convection. *Mon. Wea. Rev.*, **131**, 2394-2416.
- Cetrone, J., and R.A. Houze Jr., 2011: Leading and trailing anvil clouds of West African squall lines. *J. Atmos. Sci.*, **68**, 1114-1123.
- Chen, F., and J. Dudhia, 2001: Coupling an advanced land-surface/ hydrology model with the Penn State/ NCAR MM5 modeling system. Part I: Model description and implementation. *Mon. Wea. Rev.*, **129**, 569-585.

- 1 Chou M.-D., and M. J. Suarez, 1994: An efficient thermal infrared radiation parameterization for
2 use in general circulation models. *NASA Tech. Memo.* 104606, 3, 85pp.
- 3 Dai, A., 2006: Precipitation characteristics in eighteen coupled climate models. *J. Climate*, **19**,
4 4605-4630.
- 5 Del Genio, A.D., A.A. Lacis, and R.A. Ruedy, 1991: Simulations of the effect of a warmer
6 climate on atmospheric humidity. *Nature*, **351**, 382-385.
- 7 Del Genio, A.D., M.-S. Yao, W. Kovari and K.K.-W. Lo, 1996: A prognostic cloud water
8 parameterization for global climate models. *J. Climate*, **9**, 270-304.
- 9 Del Genio, A.D., and W. Kovari, 2002: Climatic properties of tropical precipitating convection
10 under varying environmental conditions. *J. Climate*, **15**, 2597-2615.
- 11 Del Genio, A.D., W. Kovari, M.-S. Yao and J. Jonas, 2005: Cumulus microphysics and climate
12 sensitivity. *J. Climate*, **18**, 2376-2387.
- 13 Del Genio, A.D., M.-S. Yao and J. Jonas, 2007: Will moist convection be stronger in a warmer
14 climate? *Geophys. Res. Lett.*, **34**, L16703, doi:10.1029/2007GL030525.
- 15 Del Genio, A.D., and J. Wu, 2010: The role of entrainment in the diurnal cycle of continental
16 convection. *J. Climate*, **23**, 2722-2738.
- 17 de Rooy, W.C., and A.P. Siebesma, 2008: A simple parameterization for detrainment in shallow
18 cumulus. *Mon. Wea. Rev.*, **36**, 560-576.
- 19 Donner, L.J., 1993: A cumulus parameterization including mass fluxes, vertical momentum
20 dynamics, and mesoscale effects. *J. Atmos. Sci.*, **50**, 889-906.
- 21 Donner, L.J., C.J. Seman, R.S. Hemler and S. Fan, 2001: A cumulus parameterization including
22 mass fluxes, vertical momentum dynamics, and mesoscale effects: Thermodynamic and
23 hydrological aspects in a general circulation model. *J. Climate*, **14**, 3444-3463.

- 1 Emanuel, K.A., J.D. Neelin and C.S. Bretherton, 1994: On large-scale circulations in convecting
2 atmospheres. *Q.J.R. Meteorol. Soc.*, **120**, 1111-1143.
- 3 Frederick, K., and C. Schumacher, 2008: Anvil characteristics as seen by C-POL during the
4 Tropical Warm Pool International Cloud Experiment (TWP-ICE). *Mon. Wea. Rev.*, **136**,
5 206-222.
- 6 Futyan, J.M., and A.D. Del Genio, 2007: Deep convective system evolution over Africa and the
7 tropical Atlantic. *J. Climate*, **20**, 5041-5060.
- 8 Grandpeix, J.-Y. and J.-P. Lafore, 2010: A density current parameterization coupled with
9 Emanuel's convection scheme. Part I: The models. *J. Atmos. Sci.*, **67**, 881-897.
- 10 Grandpeix, J.-Y., J.-P. Lafore and F. Cheruy, 2010: A density current parameterization coupled
11 with Emanuel's convection scheme. Part II: 1D simulations. *J. Atmos. Sci.*, **67**, 898-922.
- 12 Gregory, D., 2001: Estimation of entrainment rate in simple models of convective clouds. *Q. J.*
13 *R. Meteorol. Soc.*, **127**, 53-72.
- 14 Guichard, F., and Co-Authors, 2004: Modeling the diurnal cycle of deep precipitating
15 convection over land with cloud-resolving models and single-column models. *Q.J.R.*
16 *Meteorol. Soc.*, **130**, 3139-3172.
- 17 Hagos, S., C. Zhang, W.-K. Tao, S. Lang, Y.N. Takayabu, S. Shige, M. Katsumata, B. Olson and
18 T. L'Ecuyer, 2010: Estimates of tropical diabatic heating profiles: Commonalities and
19 uncertainties. *J. Climate*, **23**, 542-558.
- 20 Houze, R. A., Jr., and A. K. Betts, 1981: Convection in GATE. *Rev. Geophys. Space Phys.*, **19**,
21 541-576.
- 22 Houze, R.A., Jr., 1989: Observed structure of mesoscale convective systems and implications
23 for large-scale heating. *Q. J. R. Meteorol. Soc.*, **115**, 425-461.

- 1 Houze, R.A. Jr., 1993: *Cloud Dynamics*. Academic Press, San Diego, CA, 573 pp.
- 2 Houze, R.A., Jr., 1997: Stratiform precipitation in regions of convection: A meteorological
3 paradox? *Bull. Amer. Meteor. Soc.*, **78**, 2179-2196.
- 4 Houze, R.A. Jr., 2004: Mesoscale convective systems. *Rev. Geophys.*, **42**, RG4003,
5 doi:10.1029/2004RG000150.
- 6 Janjic, Z.I., 2002: Nonsingular Implementation of the Mellor-Yamada Level 2.5 Scheme in the
7 NCEP Meso model, *NCEP Office Note*, No. 437, 61pp.
- 8 Jensen, M.P., and A.D. Del Genio, 2003: Radiative and microphysical characteristics of deep
9 convective systems in the Tropical Western Pacific. *J. Appl. Meteor.*, **42**, 1234-1254.
- 10 Khairoutdinov, M., and D. Randall, 2006: High-resolution simulation of shallow-to-deep
11 convection transition over land. *J. Atmos. Sci.*, **63**, 3421-3436.
- 12 Kim, D., and Co-Authors, 2009: Application of MJO simulation diagnostics to climate models.
13 *J. Climate*, **22**, 6413-6436.
- 14 Kuang, Z., and C.S. Bretherton, 2006: A mass-flux scheme view of a high-resolution simulation
15 of a transition from shallow to deep cumulus convection. *J. Atmos. Sci.*, **63**, 1895-1909.
- 16 Laird, N.F., 2005: Humidity halos surrounding small cumulus clouds in a tropical environment.
17 *J. Atmos. Sci.*, **62**, 3420-3425.
- 18 L'Ecuyer, T.S., and G. McGarrah, 2010: A ten-year climatology of tropical radiative heating
19 and its vertical structure from TRMM observations. *J. Climate*, **23**, 519-541.
- 20 Li, W., and C. Schumacher, 2010: Thick anvils as viewed by the TRMM Precipitation Radar. *J.*
21 *Climate*, **24**, 1718-1735.
- 22 Lin, J.-L., and Co-Authors, 2006: Tropical intraseasonal variability in 14 IPCC AR4 climate

- models. Part I: Convective signals. *J. Climate*, **19**, 2665-2690.
- Mapes, B.E., 2000: Convective inhibition, subgrid-scale triggering energy, and stratiform instability in a toy tropical wave model. *J. Atmos. Sci.*, **57**, 1515-1535.
- Mapes, B., S. Tulich, J. Lin and P. Zuidema, 2006: The mesoscale convection life cycle: Building block or prototype for large-scale tropical waves? *Dyn. Atmos. Oceans*, **42**, 3-29.
- Mapes, B., and R. Neale, 2011: Parameterizing convective organization to escape the entrainment dilemma. *J. Adv. Model Earth Syst.*, **3**, M06004, doi:10.1029/2011MS000042.
- Mather, J.H., and S.A. McFarlane, 2009: Cloud classes and radiative heating profiles at the Manus and Nauru Atmospheric Radiation Measurement (ARM) sites. *J. Geophys. Res.*, **114**, D19204, doi:10.1029/2009JD011703.
- May, P.T., and D.K. Rajopadhyaya, 1999: Vertical velocity characteristics of deep convection over Darwin, Australia. *Mon. Wea. Rev.*, **127**, 1056-1071.
- May, P.T., J.H. Mather, G. Vaughan, C. Jakob, G.M. McFarquhar, K.N. Bower and G.G. Mace, 2008: The Tropical Warm Pool International Cloud Experiment. *Bull. Amer. Meteor. Soc.*, **89**, 629-645.
- Mlawer, E. J., S. J. Taubman, P. D. Brown, M. J. Iacono, and S. A. Clough, 1997: Radiative transfer for inhomogeneous atmosphere: RRTM, a validated correlated-k model for the long- wave. *J. Geophys. Res.*, **102 (D14)**, 16663–16682.
- Morrison, H., G. Thompson and V. Tatarskii, 2009: Impact of cloud microphysics on the development of trailing stratiform precipitation in a simulated squall line: Comparison of one- and two-moment schemes, *Mon. Wea. Rev.*, **137**, 991-1007.

- 1 Piriou, J.-M., J.-L. Redelsperger, J.-F. Geleyn, J.-P. Lafore and F. Guichard, 2007: An approach
2 for convective parameterization with memory: Separating microphysics and transport in
3 grid-scale equations. *J. Atmos. Sci.*, **64**, 4127-4139.
- 4 Qian, L., G.S. Young and W.M. Frank, 1998: A convective wake parameterization scheme for
5 use in general circulation models. *Mon. Wea. Rev.*, **126**, 456-469.
- 6 Rio, C., F. Hourdin, J.-Y. Grandpeix and J.-P. Lafore, 2009: Shifting the diurnal cycle of
7 parameterized deep convection over land. *Geophys. Res. Letters*, **36**, L07809,
8 doi:10.1029/2008GL036779.
- 9 Romps, D.M., and Z. Kuang, 2010: Do undiluted convective plumes exist in the upper tropical
10 troposphere? *J. Atmos. Sci.*, **67**, 468-484.
- 11 Rozbicki, J.J., G.S. Young and L. Qian, 1999: Test of a convective wake parameterization in the
12 Single-Column version of CCM3. *Mon. Wea. Rev.*, **127**, 1347-1361.
- 13 Schumacher, C., and R.A. Houze Jr., 2003: Stratiform rain in the tropics as seen by the TRMM
14 Precipitation Radar. *J. Climate*, **16**, 1739-1756.
- 15 Schumacher, C., R.A. Houze Jr. and I. Kraucunas, 2004: The tropical dynamical response to
16 latent heating estimates derived from the TRMM Precipitation Radar. *J. Atmos. Sci.*, **61**,
17 1341-1358.
- 18 Schumacher, C., and R.A. Houze, Jr., 2006: Stratiform precipitation production over sub-
19 Saharan Africa and the tropical East Atlantic as observed by TRMM. *Q.J.R. Meteorol.*
20 *Soc.*, **132**, 2235-2255.
- 21 Shige, S., Y.N. Takayabu, W.-K. Tao and C.-L. Shie, 2007: Spectral retrieval of latent heating
22 profiles from TRMM PR data. Part II: Algorithm improvement and heating estimates
23 over tropical ocean regions. *J. Appl. Met. Clim.*, **46**, 1098-1124.

- 1 Skamarock, W. C., and Co-Authors, 2008: A Description of the Advanced Research WRF
2 Version 3, NCAR Technical Note, *NCAR/TN-475+STR*, 113pp.
- 3 Tao, W.-K., and Co-Authors, 2001: Retrieved vertical profiles of latent heat release using
4 TRMM rainfall products for February 1998. *J. Appl. Meteor.*, **40**, 957-982.
- 5 Thompson, G., P. R. Field, R. M. Rasmussen, and W. D. Hall, 2008: Explicit forecasts of winter
6 precipitation using an improved bulk microphysics scheme. Part II: Implementation of a
7 new snow parameterization. *Mon. Wea. Rev.*, **136**, 5095-5115.
- 8 Tompkins, A.M., 2001: Organization of tropical convection in low vertical wind shears: The
9 role of cold pools. *J. Atmos. Sci.*, **58**, 1650-1672.
- 10 Varble, A., and Co-Authors, 2011: Evaluation of cloud-resolving model intercomparison
11 simulations using TWP-ICE observations: Precipitation and cloud structure. *J. Geophys.*
12 *Res.*, **116**, D12206, doi:10.1029/2010JD015180.
- 13 Wu, J., A.D. Del Genio, M.-S. Yao, and A.B. Wolf, 2009: WRF and GISS SCM simulations of
14 convective updraft properties during TWP-ICE. *J. Geophys. Res.*, **114**, D04206,
15 doi:10.1029/2008JD010851.
- 16 Wu, L., and G.W. Petty, 2010: Intercomparison of bulk microphysics schemes in model
17 simulations of polar lows. *Mon. Wea. Rev.*, **138**, 2211-2288.
- 18 Xie, S., and Co-Authors, 2002: Intercomparison and evaluation of cumulus parameterizations
19 under summertime midlatitude continental conditions. *Q.J.R. Meteorol. Soc.*, **128**, 1095-
20 1135.
- 21 Xie, S., T. Hume, C. Jakob, S.A. Klein, R.B. McCoy and M. Zhang, 2010: Observed large-scale
22 structures and diabatic heating and drying profiles during TWP-ICE. *J. Climate*, **23**, 57-
23 79.

- 1 Yao, M.-S., and A.D. Del Genio, 1999: Effects of cloud parameterization on the simulation of
2 climate changes in the GISS GCM. *J. Climate*, **12**, 761-779.
- 3 Yuan, J., and R.A. Houze Jr., 2010: Global variability of mesoscale convective system anvil
4 structure from A-train satellite data. *J. Climate*, **23**, 5864-5888.
- 5 Yuter, S.E., and R.A. Houze Jr., 1998: The natural variability of precipitating clouds over the
6 western Pacific warm pool. *Q.J.R. Meteorol. Soc.*, **124**, 53-99.
- 7 Zelinka, M.D., and D.L. Hartmann, 2009: Response of humidity and clouds to tropical deep
8 convection. *J. Climate*, **22**, 2389-2404.
- 9 Zelinka, M.D., and D.L. Hartmann, 2010: Why is longwave cloud feedback positive? *J.*
10 *Geophys. Res.*, **115**, D16117, doi:10.1029/2010JD013817.
- 11 Zipser, E.J., 1977: Mesoscale and convective-scale downdrafts as distinct components of squall-
12 line structure. *Mon. Wea. Rev.*, **105**, 1568-1589.
- 13 Zipser, E.J., and K.R. Lutz, 1994: The vertical profile of radar reflectivity of convective cells: A
14 strong indicator of storm intensity and lightning probability? *Mon. Wea. Rev.*, **122**, 1751-
15 1759.
- 16

FIGURE CAPTIONS

Figure 1. TRMM Precipitation Radar heating profiles composited by TRMM Microwave Imager precipitable water vapor (PW) over the tropical Indian and west Pacific Oceans. Upper left: Total CSH (left) and SLH (right) heating. Lower panels: Partitioning of SLH into convective (left) and stratiform (right) components. Dots represent the altitude of peak heating for each value of PW.

Figure 2. As in Figure 1 but for GISS GCM total diabatic minus radiative heating (upper left), convective heating (upper right), deep convective heating (lower left), and stratiform heating (lower right).

Figure 3. (Upper left) Surface rain rate and (upper right) area classification at 06Z on 20 January 2006 during the active period. The vertical and horizontal lines indicate the locations of the longitude-altitude (X-Z) and latitude-altitude (Y-Z) cross sections of (middle panels) hydrometeor mixing ratio and (lower panels) vertical velocity.

Fig. 4. Surface precipitation rate (left) and air temperature (right) at 2-hr intervals during the break period simulation.

Fig. 5. Temporal evolution of mean cold pool (solid) and non-cold pool (dashed) temperature (first row), specific humidity (second row), surface sensible heat flux (third row), and surface latent heat flux (fourth row), for the cold pools over ocean (left panels) and land (right panels).

Fig. 6. Observed surface temperature time series at Howard Springs station (~25 km east of Darwin) during the TWP-ICE monsoon break period, showing the effect of a cold pool

associated with passage of a storm at 22 LST on 10 February 2006. The dotted vertical lines show the onset and termination of the cold pool event at the station.

Figure 7. Simulated 10-minute average vertical velocity field at (upper) 600 m and (lower) 2 km altitude at 06Z on 10 February 2006.

Figure 8. Vertical profiles of mean TR (upper) and SR (lower) region temperature anomalies relative to the domain mean for the active monsoon period simulations with the Morrison et al. (2009) (left) and Thompson et al. (2008) (right) microphysics.

Figure 9. Vertical velocity distributions (percentiles) vs. pressure for the CU (left), TR (middle), and SR (right) regions in the active period simulations with the Morrison et al. (2009) (upper) and Thompson et al. (2008) (lower) microphysics.

Figure 10. As in Figure 9 but for mean profiles of the mixing ratio of different hydrometeor types.

Figure 11. Lag correlation between (upper) 600-200 hPa mean relative humidity and TR or SR area, and between (lower) 600-200 hPa mean vertical shear of horizontal wind and TR or SR area in the active period simulations with the (left) Morrison et al. and (right) Thompson et al. microphysics. A correlation of 0.25 is significant at the 95% level.

Figure 12. As in Figure 11 but for correlations between cumulus mass flux and TR or SR area for the (upper) active and (lower) break periods with both microphysics schemes. For the break period, a correlation of ~ 0.3 - 0.4 (increasing with lag) is significant at the 95% level.

Figure 13. As in Figure 11 but for correlations between (upper) cumulus mass flux and TR or SR hydrometeor mixing ratio and between (lower) cumulus updraft speed and TR or SR hydrometeor mixing ratio during the active period.

1 Figure 14. (Left) CU/TR/SR classification as in Figure 3 and (right) 600 hPa relative humidity
2 during the (upper) active period and (lower) break period.

3

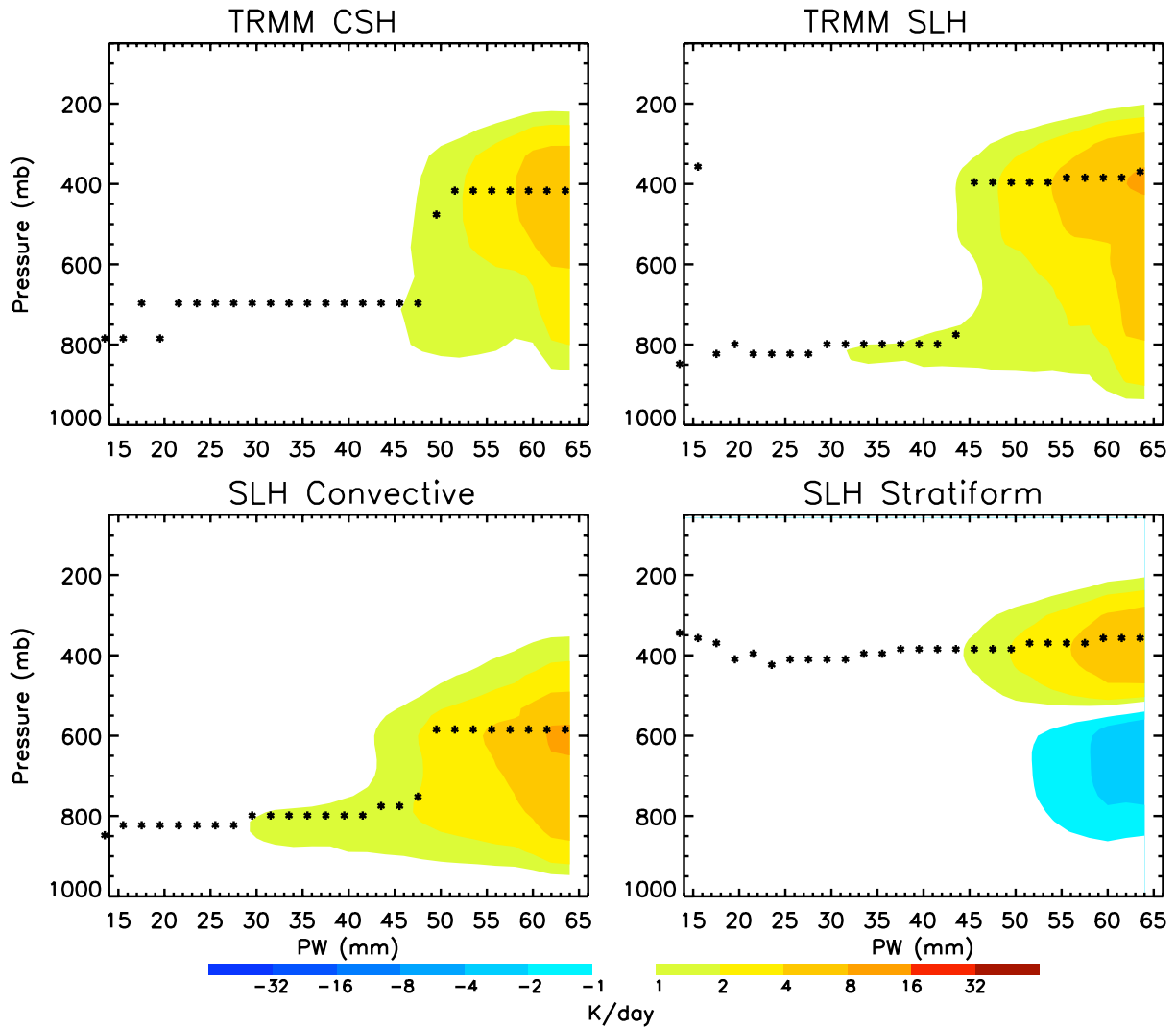


Figure 1. TRMM Precipitation Radar heating profiles composited by TRMM Microwave Imager precipitable water vapor (PW) over the tropical Indian and west Pacific Oceans. Upper left: Total CSH (left) and SLH (right) heating. Lower panels: Partitioning of SLH into convective (left) and stratiform (right) components. Dots represent the altitude of peak heating for each value of PW.

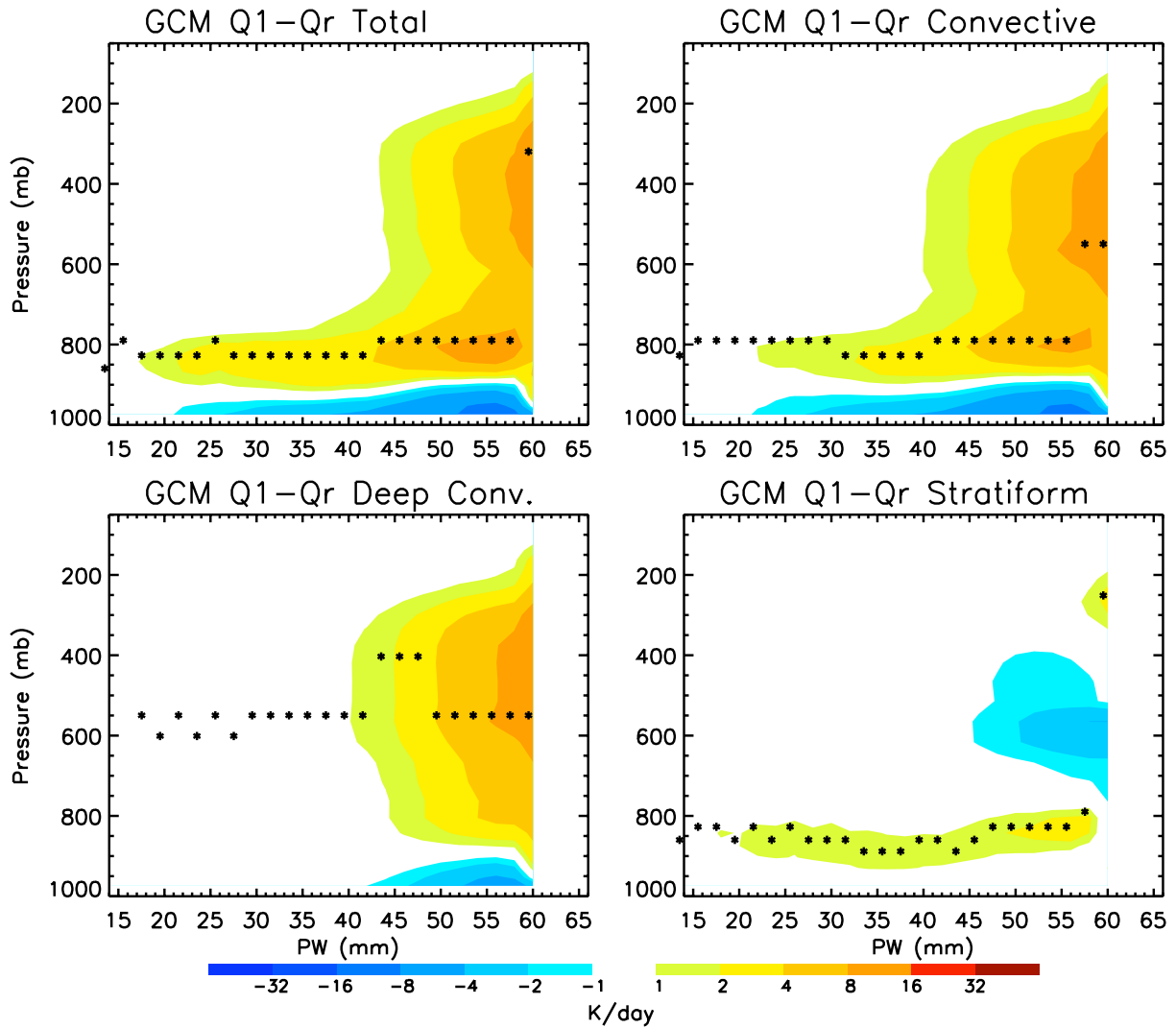


Figure 2. As in Figure 1 but for GISS GCM total diabatic minus radiative heating (upper left), convective heating (upper right), deep convective heating (lower left), and stratiform heating (lower right).

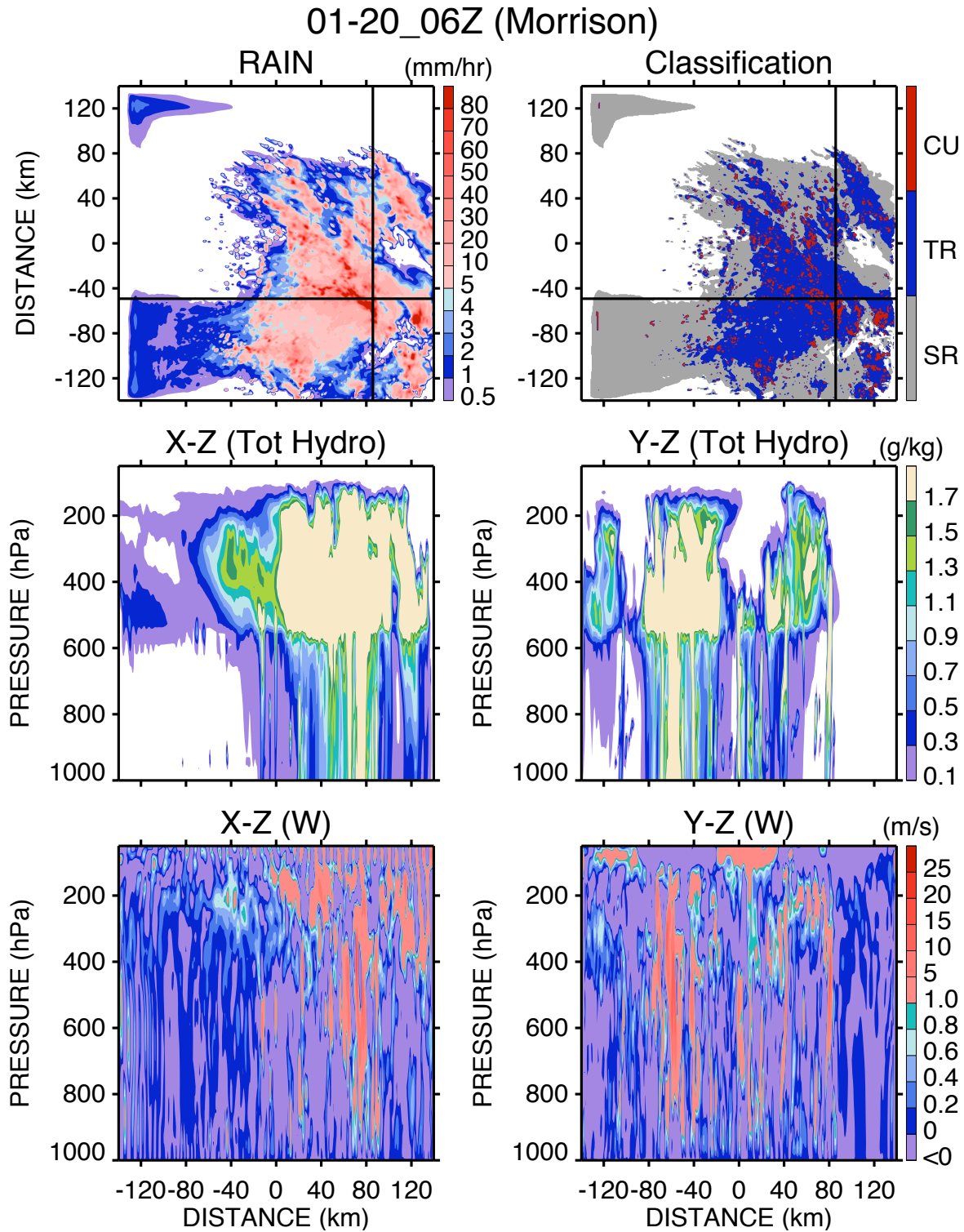


Figure 3. (Upper left) Surface rain rate and (upper right) area classification at 06Z on 20 January 2006 during the active period. The vertical and horizontal lines indicate the locations of the longitude-altitude (X-Z) and latitude-altitude (Y-Z) cross sections of (middle panels) hydrometeor mixing ratio and (lower panels) vertical velocity.

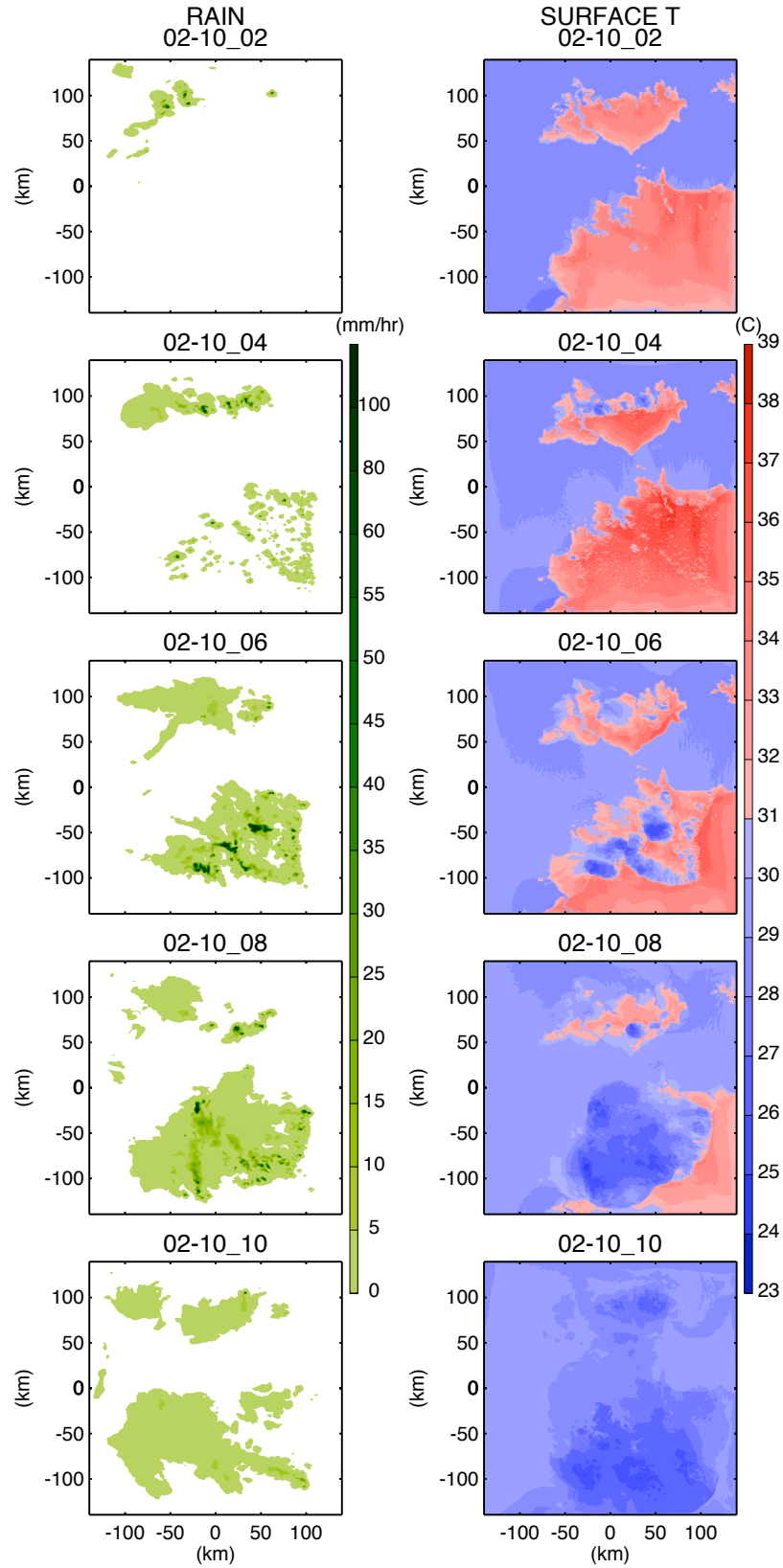


Fig. 4. Surface precipitation rate (left) and air temperature (right) at 2-hr intervals during the break period simulation.

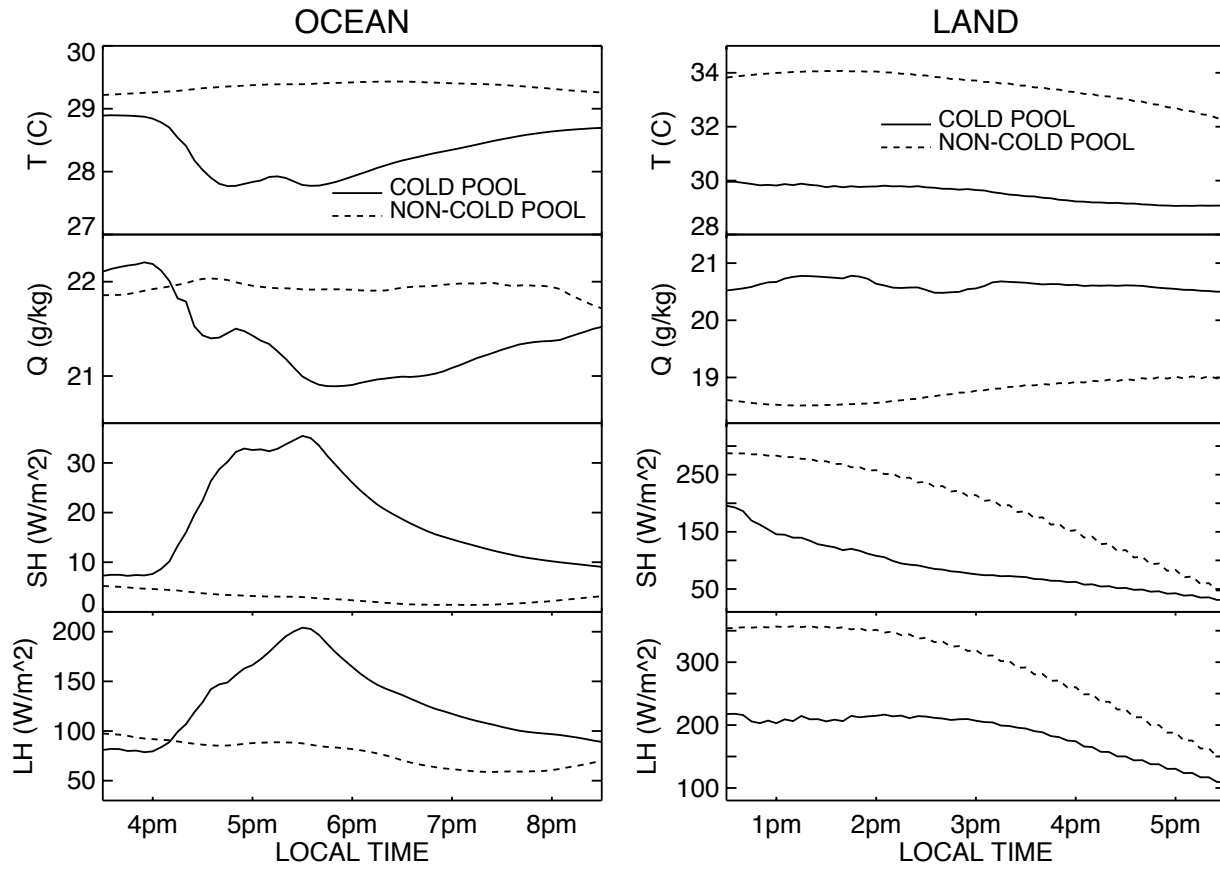


Fig. 5. Temporal evolution of mean cold pool (solid) and non-cold pool (dashed) temperature (first row), specific humidity (second row), surface sensible heat flux (third row), and surface latent heat flux (fourth row), for the cold pools over ocean (left panels) and land (right panels).

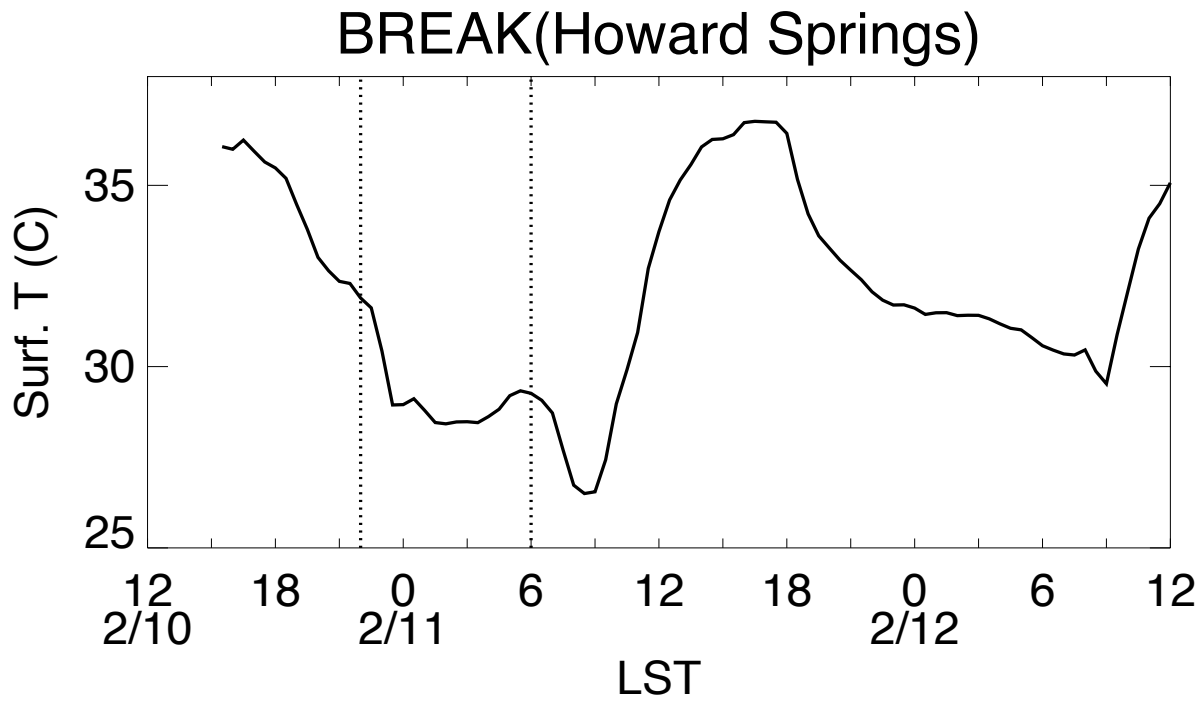


Fig. 6. Observed surface temperature time series at Howard Springs station (~25 km east of Darwin) during the TWP-ICE monsoon break period, showing the effect of a cold pool associated with passage of a storm at 22 LST on 10 February 2006. The dotted vertical lines show the onset and termination of the cold pool event at the station.

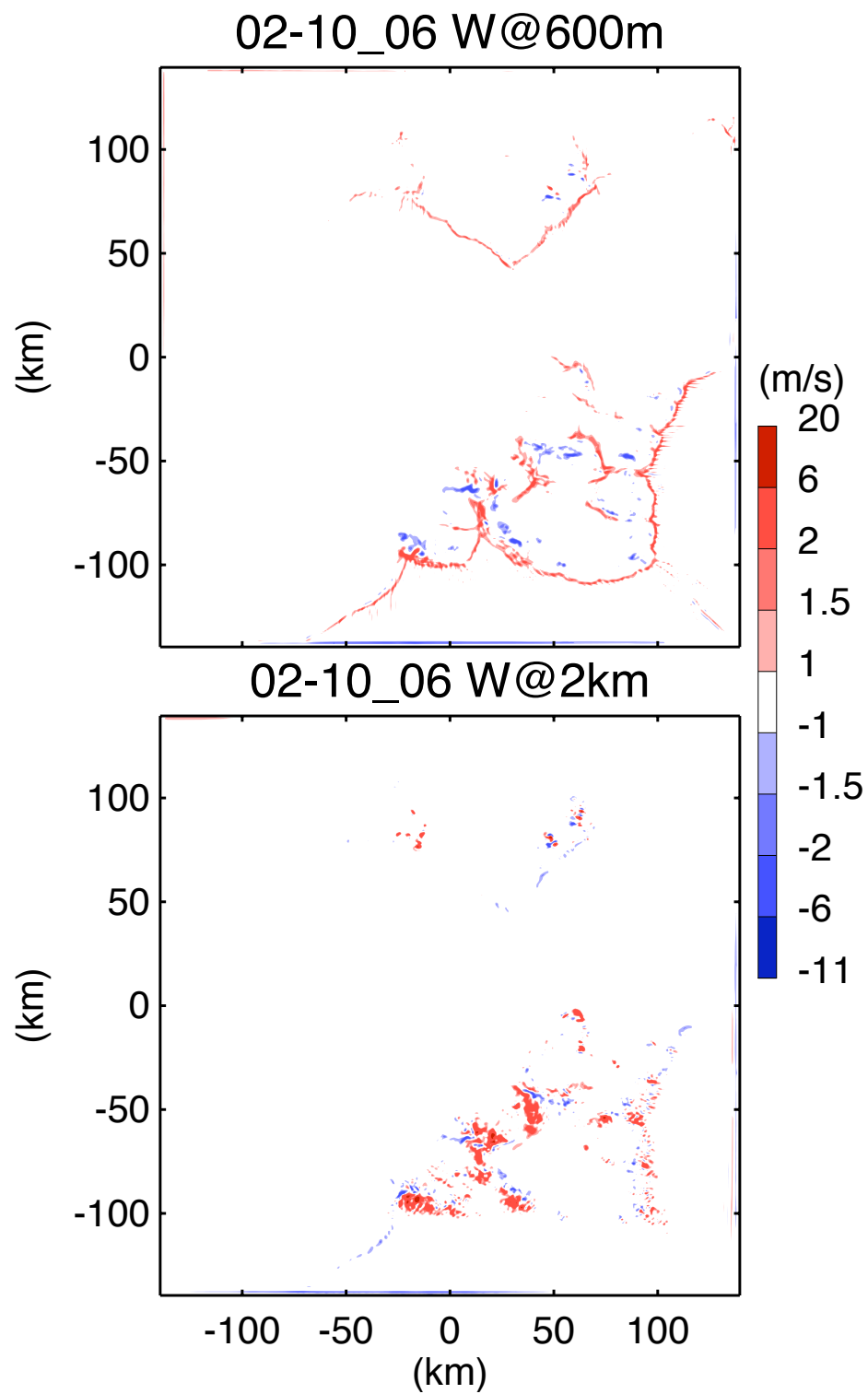


Figure 7. Simulated 10-minute average vertical velocity field at (upper) 600 m and (lower) 2 km altitude at 06Z on 10 February 2006.

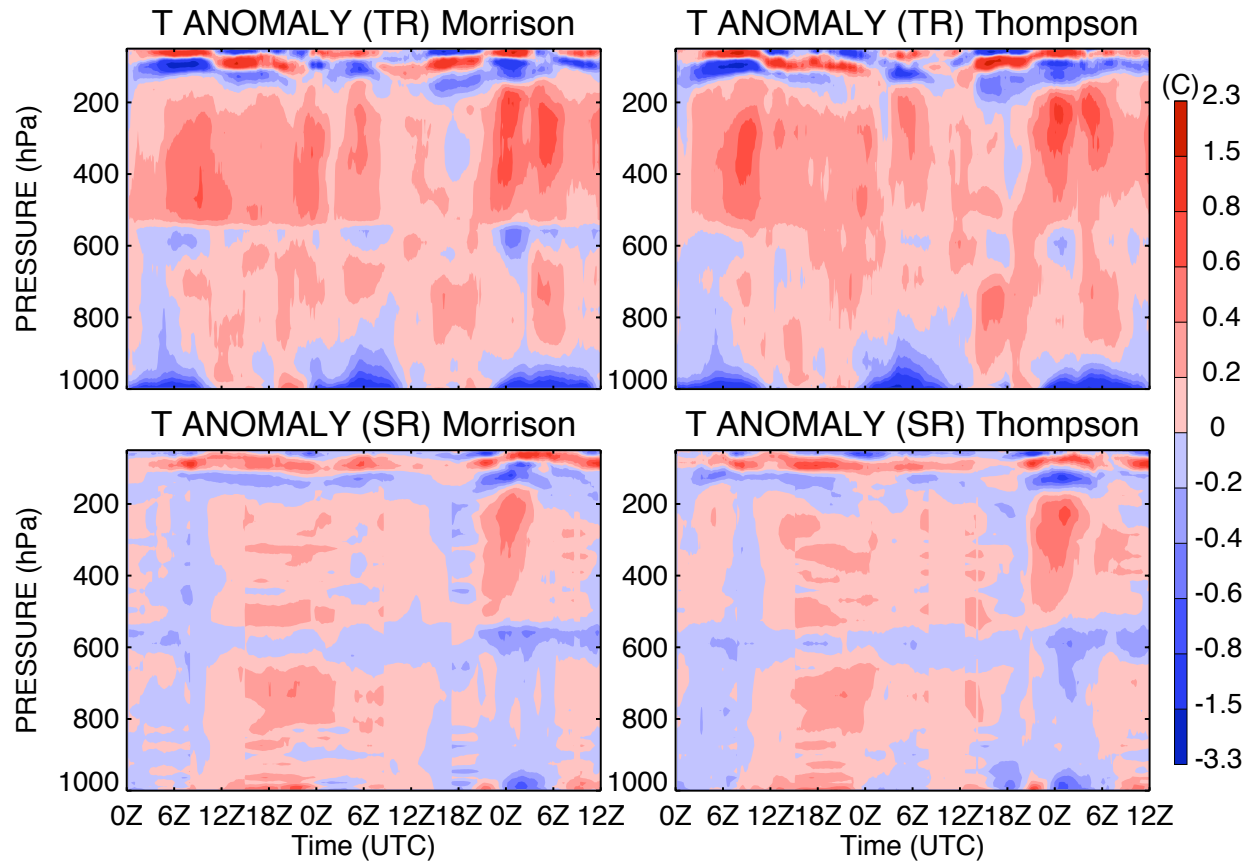
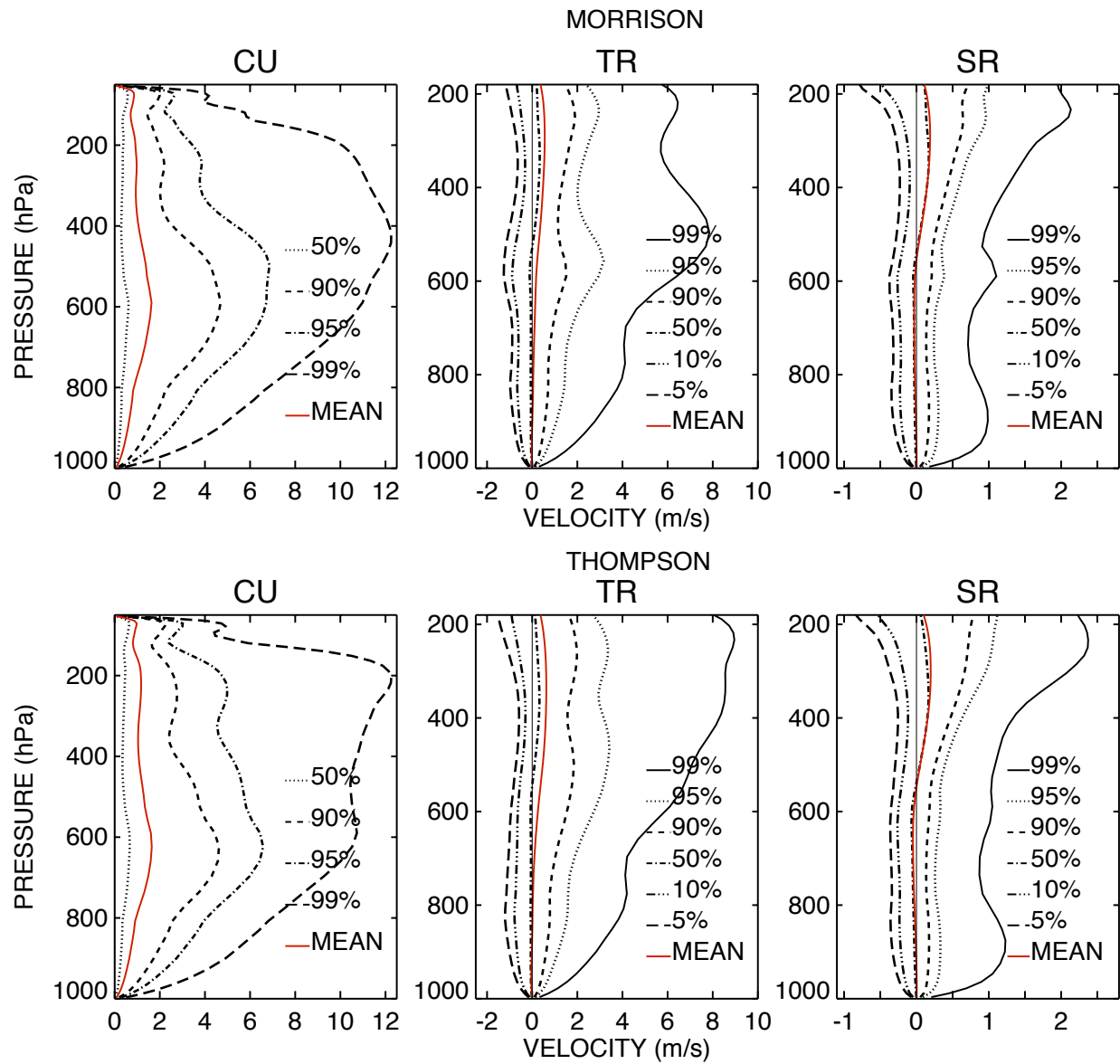


Figure 8. Vertical profiles of mean TR (upper) and SR (lower) region temperature anomalies relative to the domain mean for the active monsoon period simulations with the Morrison et al. (2009) (left) and Thompson et al. (2008) (right) microphysics.

1



2

3 Figure 9. Vertical velocity distributions (percentiles) vs. pressure for the CU (left), TR (middle),
 4 and SR (right) regions in the active period simulations with the Morrison et al. (2009) (upper)
 5 and Thompson et al. (2008) (lower) microphysics.

6

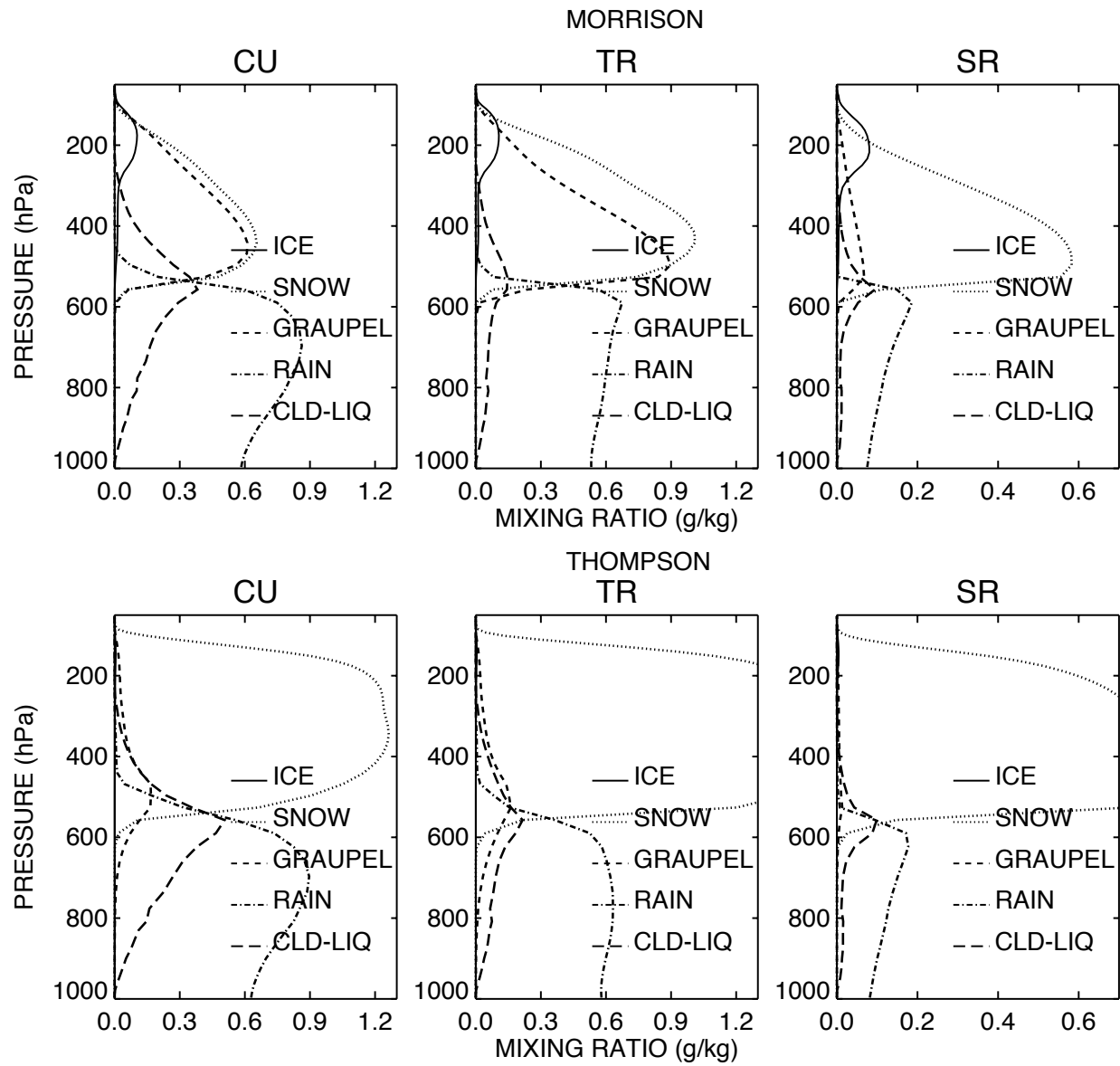


Figure 10. As in Figure 9 but for mean profiles of the mixing ratio of different hydrometeor types.

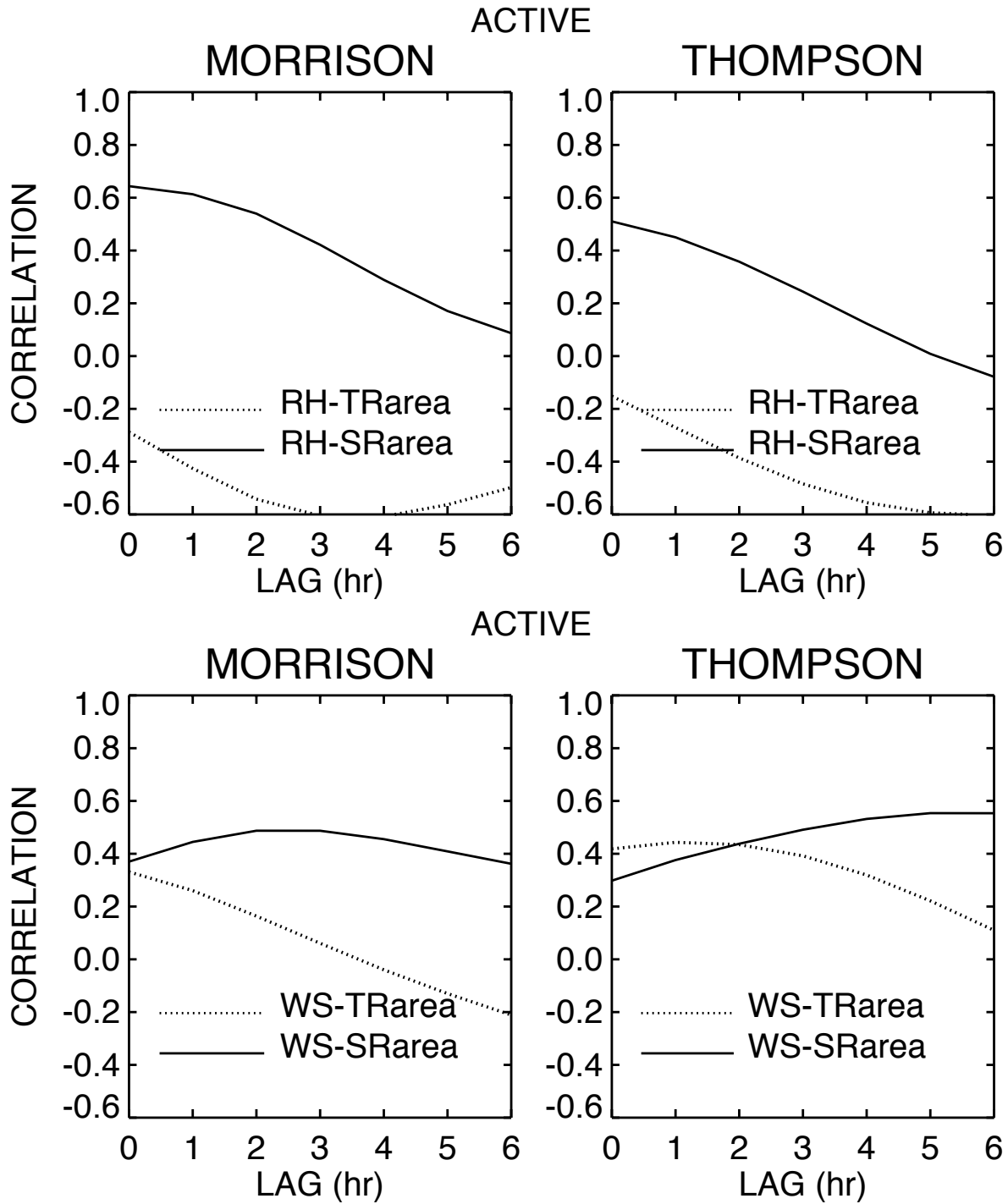
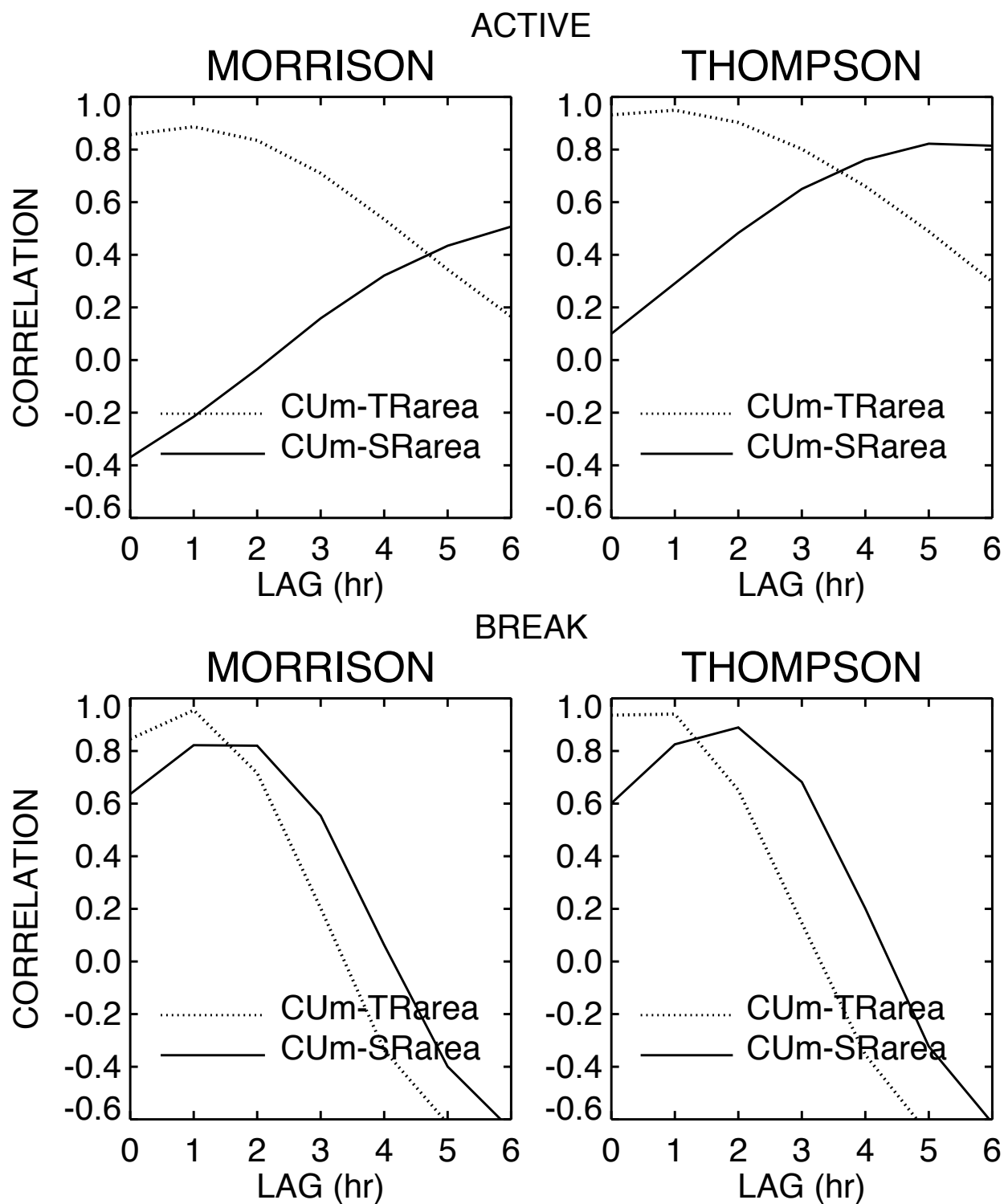


Figure 11. Lag correlation between (upper) 600-200 hPa mean relative humidity and TR or SR area, and between (lower) 600-200 hPa mean vertical shear of horizontal wind and TR or SR area in the active period simulations with the (left) Morrison et al. and (right) Thompson et al. microphysics. A correlation of 0.25 is significant at the 95% level.



2

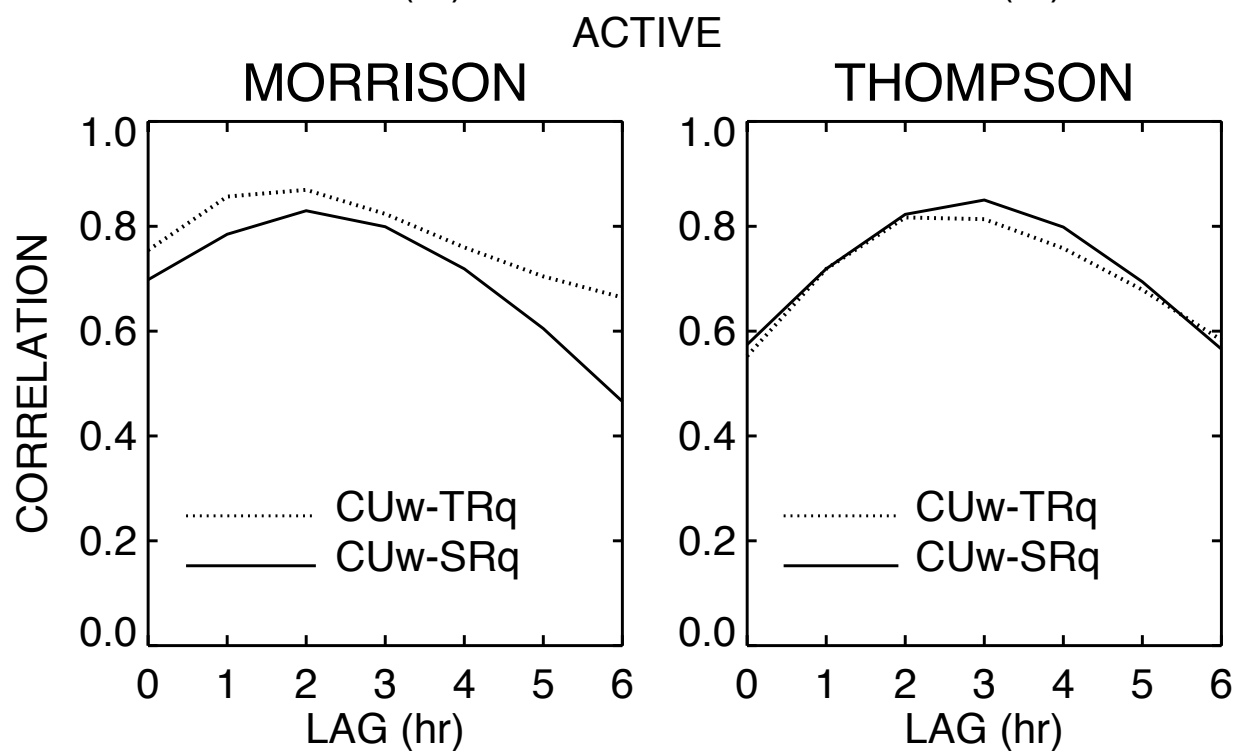
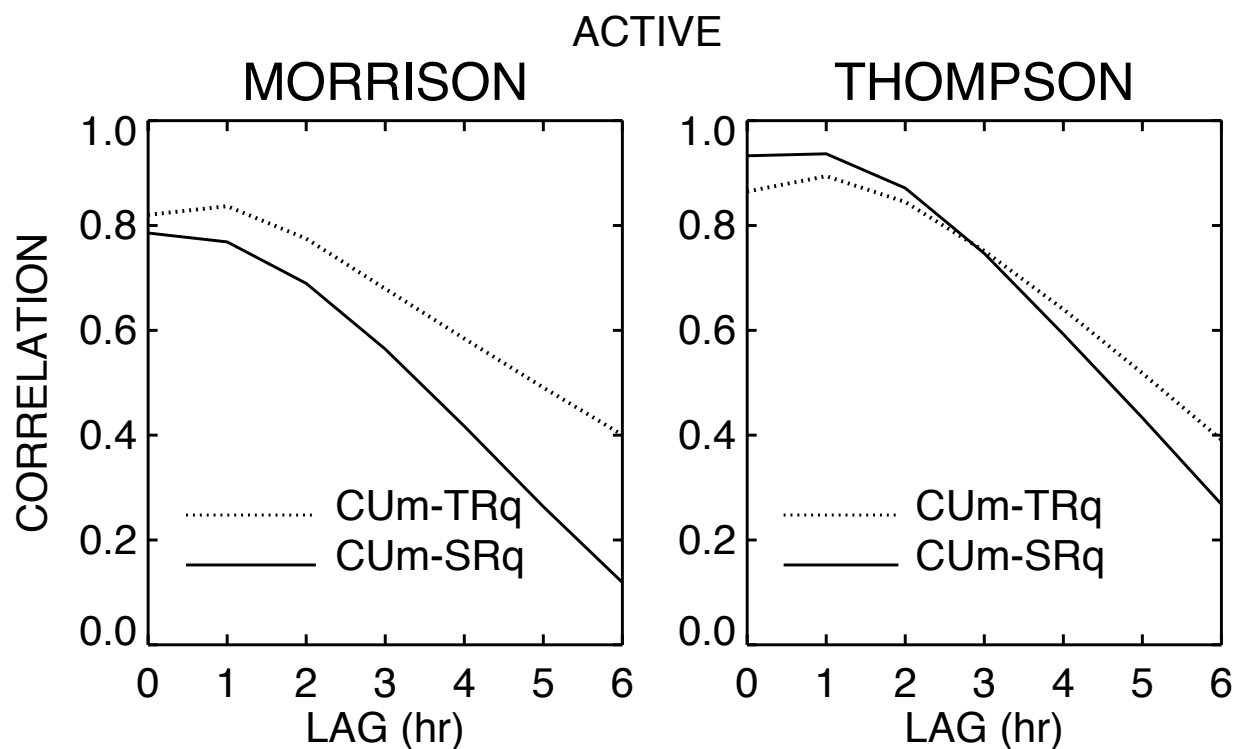
3 Figure 12. As in Figure 11 but for correlations between cumulus mass flux and TR or SR area

4 for the (upper) active and (lower) break periods with both microphysics schemes. For the break

5 period, a correlation of ~ 0.3 - 0.4 (increasing with lag) is significant at the 95% level.

6

1



2

3 Figure 13. As in Figure 11 but for correlations between (upper) cumulus mass flux and TR or
 4 SR hydrometeor mixing ratio and between (lower) cumulus updraft speed and TR or SR
 5 hydrometeor mixing ratio during the active period.

6

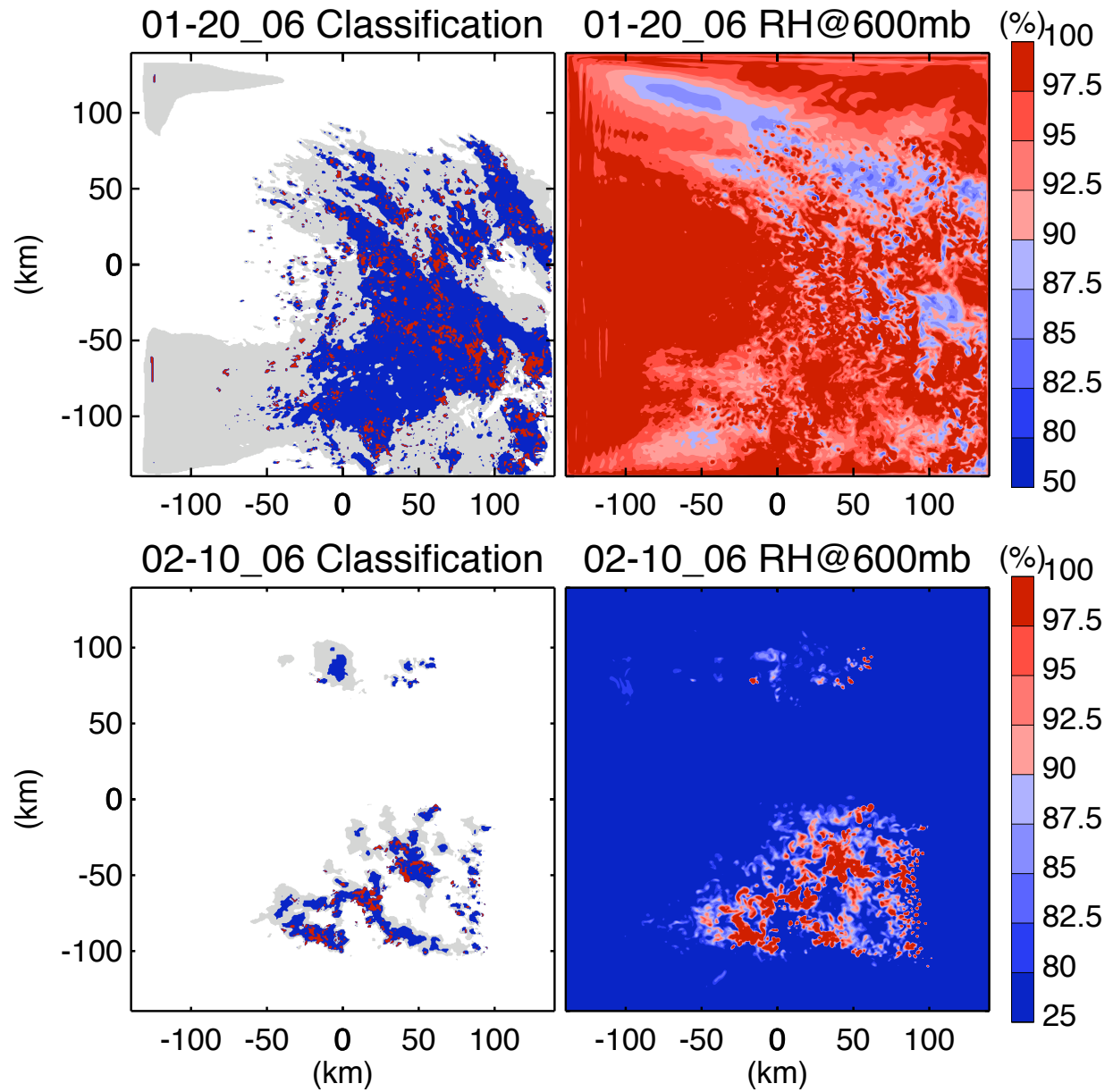


Figure 14. (Left) CU/TR/SR classification as in Figure 3 and (right) 600 hPa relative humidity during the (upper) active period and (lower) break period.

Table 1. Percent area covered by deep convection (CU), transition rain (TR), and stratiform rain (SR) during the active monsoon and monsoon break simulations with different microphysics parameterizations. The observations are from Frederick and Schumacher (2008), who do not define a separate transition rain category.

Region	Active Monsoon			Monsoon Break		
	Morrison	Thompson	Observed	Morrison	Thompson	Observed
CU	3.2	3.1	8.6	0.2	0.2	2.2
TR	10.9	9.5		1.2	0.8	
SR	40.3	34.3	33.2	2.4	1.6	5.6
Total	54.4	46.9	41.8	3.8	2.6	7.8

1 Table 2. 600 hPa mean relative humidity (%) over different parts of the domain for the
2 simulated active monsoon and monsoon break periods using the Morrison et al. (2009)
3 microphysics.

4

Region	Active Monsoon	Monsoon Break
CU	98.8	94.4
TR	96.3	82.2
SR	96.0	77.3
Domain	96.5	66.4

5